**Department of Precision and Microsystems Engineering**

# Atalanta Flying Prototype: The Design, Fabrication and Testing of an Uncontrolled Resonant Flapping-Wing Micro Air Vehicle using a Linear Frequency Divider

By Mike Menkhorst

Report no : 2023.040
Coach : Dr. ir. H. Goosen
Professor : Dr. ir. H. Goosen
Specialisation : High Tech Engineering
Type of report : Technical Report
Date : 21 June 2023

# Atalanta Flying Prototype

## The Design, Fabrication and Testing of an Uncontrolled Resonant Flapping-Wing Micro Air Vehicle using a Linear Frequency Divider

by

Mike Menkhorst

to obtain the degree of Master of Science
at the Delft University of Technology,
to be defended publicly on Wednesday 21, June at 14:00 PM.


| | | |
|---|---|---|
| Student number: | 4563972 | |
| Project duration: | September 1, 2021 – June 21, 2023 | |
| Thesis committee: | Dr. ir. H. Goosen, | TU Delft, supervisor |
| | Prof. dr. ir. J.L. Herder, | TU Delft, Exam commitee |
| | M.Sc. Serena Basile, | TU Delft, Phd |


An electronic version of this thesis is available at `http://repository.tudelft.nl/`.

TU Delft

# Abstract

Drones are becoming an ever increasing part of our lives. From airshows to surveillance systems, their use varies greatly and, as technology improves, this variety will continue to increase. As drones get smaller, new applications arise. For example, drones for monitoring crops or searching for survivors in hard to reach places in disaster areas. One of the main fields of improvement to drone design is energy efficiency. The more energy efficient a drone is, the longer it can fly and the more it can carry. This is the objective of the Atalanta project. It seeks to develop a drone with a wingspan smaller than 15 cm and an improved energy efficiency over other drones. It does this by two means. Firstly, it uses a bio-inspired flapping wing solution, mimicking the methods used by insects to fly. This carries a greater efficiency over the more ubiquitous rotary wing design. Secondly, it looks to apply resonance, allowing more energy conservation between wing flaps.

In its current state, the Atalanta project has gathered an expansive amount of theoretical knowledge, but lacks the validation a prototype would provide. This report gathered the knowledge contained within the Atalanta project and supplemented it with new information generated in the last two years. It identified three main challenges to overcome and provided a set of guidelines to overcome them. The challenges are as follows: Firstly, the total design is too heavy for the theoretical lift generated by the wings. Secondly, the wings, in their current form, are too heavy for an actuator to operate at the right frequency. Thirdly, little documentation exists on the design of the resonant element the design has to be built around. If all three of these challenges are addressed, it should be possible to create a flying prototype for the Atalanta project using an external power source and external control.

To overcome the limits of the generated lift, varying actuators were evaluated. As no actuator was found meeting the projects requirements, a gearbox solution was sought instead. Through the use of a linear frequency divider, the available power from an actuator could be doubled by doubling the operating frequency of the actuator without changing the flapping frequency of a wing. A linear frequency divider was developed for this purpose. As this element also fulfills the role of the Atalanta body, the third challenge was also addressed through this element by designing it to function as a resonant element, vibrating at the desired frequency. This linear frequency divider was successfully developed, but was unable to be integrated into the prototype within the available time.

To address the weight of the wings, a vacuum forming method was investigated. By applying heat to a film of plastic and pulling it over a mold using a vacuum, a wing of a desired shape can be created. By introducing localised folds in this wing, it can be reinforced and be made stiffer. Although this seemed promising, no suitably light wing was produced using this method, but further research is likely to produce positive results. As only mylar was investigated in this paper, evaluation of other materials could prove productive. Alternatively, using a combination of vacuum forming and local reinforcements may well create a near rigid wing.

Despite the increase in losses due to the heavier than desired wings, the drone presented in this paper could theoretically fly for short periods of time, as the losses of the flight are compensated for by the energy provided by the used actuator. It was originally predicted that the Atalanta would have a power density requirement of 30 W/kg. Despite the heavier wings and the increase in weight from the components added by the linear frequency divider, the new loss to mass ratio is only 38.4 W/kg. The weight of the prototype has increased as well, however. Despite all this, the actuator is predicted to be able to deliver 1.15 watts of power with the losses being 0.713 watts. As such, with the addition of the linear frequency divider, the prototype can theoretically fly, if integrated properly. Also of note is the lack of optimisation for the linear frequency divider. As this is the first paper investigating this part, a substantial amount of time was spent evaluating the effectiveness of the part. As such, further investigation in this area could lead to further optimisation or even the inclusion of a second divider, allowing the frequency of the actuator, therefore its power, to be doubled again.

# Preface

This report details the progress and results of my master thesis as part of the track High-Tech Engineering at the faculty of Mechanical, Maritime and Materials Engineering at Delft University of Technology. This project is carried out within the Department of Precision and Microsystems Engineering with Dr.Ir. Hans Goossen as supervisor.

Over the course of my master I put great focus on subjects involving system engineering. As such, when an assignment to unify multiple projects into a functioning bio-inspired prototype was presented to me, it felt like the project was made for me. Furthermore, being handed more than of a decade of prior research, the prospect of creating the first flying prototype for the Atalanta project is more than I could have hoped for when selecting my master thesis.

I would like to thank Hans for his guidance and support during this project as well as my predecessors who facilitated this project.

Lastly, I would like to wish any of my successors good luck with the continuation of this project.

Mike Menkhorst
Delft, June 2023

# Contents

# 1 Introduction

Drones have begun to see an ever increasing use in our lives over the past few years. These uses range from airshows of hundreds of drones lighting up the sky, to drones capable of delivering packages, to military models used for surveillance and strike capabilities. The use and application is widespread. In the future we might see drones that aid in disaster relief, agriculture or firefighting [1]. These drones could aid rescue workers in finding survivors in areas too narrow for rescue workers to enter, monitor crops while administering pesticides, and help firefighters determine the direction and spread of fires. A challenge for many drone applications is refined control in confined spaces as well as the energy efficiency of the drone. This report focuses on this facet of drone operation.

Before proceeding with the subject matter of this report in greater detail, it is useful to be able to differentiate different types of drones. A drone is classified as an unmanned aerial vehicle that is operated remotely or autonomously and capable of carrying payloads. Within this classification multiple sub-types exist. These can be differentiate by weight, wingspan and range. The drone classifications of relevance to this report are the micro air vehicle (MAV) and the nano air vehicle (NAV). The standard dimensions for these aerial vehicles (AVs) were defined by the US Defense Advanced Research Products Agency (DARPA). MAVs have a wingspan under 15 cm and NAVs under 7.5 cm [2]. This paper will focuses on MAVs.

MAVs can be divided into three groups. These are fixed-wing MAVs (FMAV), rotary-wing MAVs (RMAV) and flapping-wing MAVs (FWMAV). FMAVs operate by generating an airflow over a fixed surface to generate lift in a similar manner to commercial aircraft. A big downside of FMAVs is the required velocity for sufficient lift, severely limiting the hovering capability and typically limits the direction of flight. This makes FMAVs unsuited for confined applications, such as indoors. RMAVs and FWMAVs do not have this downside. RMAVs operate using a rotating surface area, allowing the generation of thrust and lift in a similar manner to a helicopter. A downside is that this requires multiple actuators to enable control and negate spin, increasing the RMAVs weight. FWMAVs operate using principles inspired by insects. By moving the lift generating surface back and forth, the FWMAV can generate lift and thrust similar to the RMAV, but where a RMAV needs at least two similar actuators to negate the spin generated by its operation, a FWMAV may need only one actuator for the generation of thrust and lift. Additionally, FWMAVs have the best force per wing surface performance. This makes FWMAVs appealing for further research [2] [3].

In the following sections FWMAVS will be discussed, an introduction to the Atalanta project will be given together with the goals of this report and the report will be outlined.

## 1.1. Existing Flapping-Wing Drones

Multiple flapping-wing drones capable of flight have already been developed. These include the DelFly Nimble with a wingspan of 33 cm, weighing 27 g. This drone is capable of 5 minutes of flight, travelling one kilometer [4]. At 33 cm, the DelFly does not classify as an MAV. An example of a FWMAV is Havard University's RoboBee X-wing with a wingspan of under 5 cm and weighing less than 500 mg. In 2020 it achieved flight without requiring an external power source. Using miniature photo-voltaic cells it generates its own power during flight. This allowed the RoboBee to generate short bursts of lift [5].

Most interesting might be the DelFly Micro. With a wingspan of 10 cm and a mass of 3.07 g, it manages a range of 50 m [6]. This makes it one of the best examples of a FWMAV available at this time. A major

downside to this design, however, is the fact it has lost the capacity to hover in place, due to its weight-to-lift ratio, requiring a velocity to maintain lift.

These examples show us that drones capable of operating in confined spaces need better energy efficiency, energy storage and control.

## 1.2. Atalanta Project

The Atalanta project looks to create a FWMAV with a resonant transmission system mimicking the indirect flapping mechanism found in insects. This is expected to lead to a system with a high efficiency by storing the energy normally lost to reversing the velocity of the wings in a spring element. Additionally, the resonant properties allow the use of a less powerful actuator compared to none resonant FWMAVs. This is due to the fact that forces necessary to move the wings is generated by the spring element, rather than the actuator. The actuator only needs to provide the power lost to drag and friction in each flap. The Atalanta FWMAV is expected to have a wingspan of 10 cm and a mass of up to 8.85 g, as predicted by Bolsman. A FWMAV design for the Atalanta project will have the following properties as outlined by Bolsman [7]:

- Fly autonomously
- Maintain lift at low speeds (hover)
- Communicate with an external controller
- Autonomously store power
- Carry a payload
- Be adaptable for many situations

In addition to those properties, as these merely constitute a hover-capable drone, an Atalanta FWMAV includes the following additional properties:

- Use a flapping wing approach to achieve lift
- Have a wingspan of under 15 cm to fall within the definition of a MAV
- Use compliance and resonance to decrease power usage

## 1.3. Problem Description

This research seeks to test the viability of the Atalanta project in its current theoretical state. It mainly looks into the design and fabrication process of the wings, hinge and the body of the FWMAV, as well as what actuator would be best suited for this design. It then seeks to test the flight capacity of this system, excluding elements for control or payload in this system. The design topic is the following:

- Design, fabricate and test a mechanism that, through the use of flapping wings, can achieve sufficient lift to overcome its own weight while retaining a wingspan under 15 centimeters.

A full list of design criteria can be found in Chapter 3.1. It is important to note that this design does not classify as a drone, due to lacking autonomy and a payload.

## 1.4. Report Outline

This report will first outline the information gathered by the Atalanta project to date, as well as new papers published since 2018. Using this, it seeks to assess the challenges and viability for the completion of the design topic. Next, it translates this information to a list of requirements and eliminates design options that fail to be viable. This is followed by an analysis of the chosen design options, allowing the creation of a prototype. This is followed by an analysis of manufactured prototypes. Finally, recommendations and conclusions are presented.

# 2

# State of the Art

The following chapter will explore the information currently gathered by the Atalanta project, as well as add any knowledge that is currently lacking for the purposes of designing a working prototype.

The following sources were used to inform the following sections:

- PME Reports - The TU Delft repository provides multiple reports as part of the Atalanta project. These papers and the references therein were used to form a foundation.
- Google Scholar was used to gather more recent information. For this, emphasis was placed on papers published after 2018 and on resonant systems.

## 2.1. State of MAV Design

In Table 2.1 a list of flapping wing designs has been compiled.

Most flapping wing MAVs use DC motors as their actuators, followed by piezoelectric actuators. DC motors provide a simple and reliable means of generating the necessary forces to flap the wings, while piezoelectric actuators offer higher power-to-weight ratios and can operate at higher frequencies than DC motors. Other types of actuators, such as linear solenoids, have also been used in some MAV designs.

In terms of flight capabilities, some MAVs are capable of sustained flight, while others are limited to hovering or short flights. Many of the more recent designs have focused on improving flight endurance and maneuverability, which are key requirements for many applications. For example, the Hummingbird MAV developed by AeroVironment[8] is capable of sustained flight for up to 10 minutes, while the Delfly Nimble can perform agile maneuvers and motions, at the cost of hovering capability.

Despite the advances made in MAV design, there are still many challenges that need to be addressed. One major challenge is the development of power sources that are small and lightweight enough to be carried by the MAVs, yet provide sufficient energy for sustained flight. Another challenge is the development of control systems that enable the MAVs to operate autonomously in complex and dynamic environments.

Overall, flapping wing MAVs represent a rapidly evolving field of research and development, with many advances being made in both design and applications. As the technology continues to mature, it is likely that these flying robots will become increasingly useful in a wide range of fields, from disaster response to environmental monitoring to military reconnaissance.

| MAV | Actuator | Actuator Mass | Wingspan | Mass | Flight | Year | Ref |
|---|---|---|---|---|---|---|---|
| Atalanta | Linear Solenoid | 5.5 g | 10 cm | 7 g | No | 2020 | [9] |
| Microbat | DC motor | 3 g | 23 cm | 14 g | Yes | 2003 | [10] |
| MFI | Piezo | 1 g | 2.5 cm | 9.81 g | No | 2007 | [11] |
| LIPCA MAV 1 | Piezo | 6.10 g | 12.5 cm | 10.38 g | No | 2007 | [12] |
| LIPCA MAV 2 | Piezo | 6.10 g | 12.5 cm | 10.28 g | No | 2008 | [13] |
| Microfly | Piezo | 0.04 g | 3 cm | 0.06 g | Yes | 2008 | [14] |
| Resonant Robot | DC motor | Unknown | 10 cm | 5.8 g | No | 2009 | [15] |
| Delfly 2 | DC motor | Unknown | 28 cm | 16 g | Yes | 2012 | [16] |
| Delfly Micro | DC motor | 0.6 g | 10 cm | 3.07 g | Yes | 2012 | [6] |
| Nano Hummingbird | DC motor | Unknown g | 7.5 cm | 19 g | Yes | 2012 | [17] |
| RoboBee | Piezo | Unknown g | 3 cm | 0.08 g | Yes | 2013 | [18] |
| Carnegie MAV 1 | DC motor | Unknown | 8 cm | 6.8 g | No | 2013 | [19] |
| Carnegie MAV 2 | DC motor | 1.21 g | 20 cm | 2.7 g | Yes | 2014 | [20] |
| Jellyfish Flyer | DC motor | 1.1 g | 16 cm | 2.1 g | Yes | 2014 | [21] |
| Carnegie MAV 3 | Piezo | 0.13 g | 7 cm | 0.65 g | No | 2014 | [22] |
| Carnegie MAV 4 | DC motor | Unknown | 21 cm | 6.9 g | Yes | 2015 | [23] |
| Hummingbird | DC Motor | 16.8 g | 30.48 cm | 62 g | Yes | 2015 | [8] |
| Harvard MAV | DC motor | 1.217 | 8 cm | 3.2 g | Yes | 2016 | [24] |
| KUBeetle | DC motor | 3.5 g | 16 cm | 21 g | Yes | 2017 | [25] |
| Colibri | DC motor | 4.19 g | 21 cm | 22 g | Yes | 2017 | [26] |
| Delfly Nimble | DC motor | 1.43 g | 33 cm | 29 g | Yes | 2018 | [4] |
| RoboBee X-wing | Piezo | Unknown | 3.5 cm | 0.259 g | Yes | 2019 | [5] |
| DEA MAV | Dielectric | 0.12 g | 10.6 cm | 0.6-1.2 g | No | 2019 | [27] |
| Dichtoma MAV | DC motor | 7.8 g | 19 cm | 23.1 g | Yes | 2020 | [28] |
| Cross Coupling MAV | Piezo | 0.116 g | 10 cm | 1.12 g | Yes | 2020 | [29] |
| Piezo MAV | Piezo | Unknown | 11.5 cm | 1.15 g | Yes | 2020 | [30] |

Table 2.1: List of MAV designs

## 2.2. The Atalanta Project

The Atalanta project current consists of 32 reports: 4 literature surveys, 3 PhD theses, 8 bachelor end projects and 17 Master theses. A full list of these reports can be found in Appendix A. These reports are ordered by subject and publishing year. Of particular note are the reports "Flapping wing actuation using resonant compliant mechanisms: An insect-inspired design" by Casper Bolsman [7] and the literature study "Design, Fabrication and Testing of a Resonant Flapping-Wing Micro Air Vehicle" by Meindert Ras [31]. The former lays out a broad analysis on the potential for resonance when used in FWMAVs. The latter compiles the Atalanta research up to 2019.

### 2.2.1. Resonance

Atalanta is heavily inspired by the mechanisms that insects use to fly. Of consideration are three main body parts of insects; the head, the thorax and the abdomen. If we compare these parts to that of a FWMAV, similarities arise. The head is similar to a control and sensor circuit, and the abdomen is similar to the energy storage mechanism. Of most interest is the thorax. This structure acts as the actuation mechanism for the wings. Two topographies exist for the thorax. The first topology is a direct approach. Here the muscles are attached to the wings. As such, this allows an insect to operate each of its wings independently. The obvious downside is the increased number of actuators/muscles required (one for each wing), but also a smaller stroke amplitude as you can't enlarge the stroke mechanically. The second topology is the indirect approach as seen in Figure 2.1. Here the muscles are attached to the shell of the elastic thorax. One set of muscles drives the upward movement, the other the downward movement of the wings. Due to the elastic properties of the thorax, the system can be represented as a mass-spring-damper system. Due to the resonant properties and larger strokes of the indirect system, it is used for the purposes of the Atalanta project. [7]

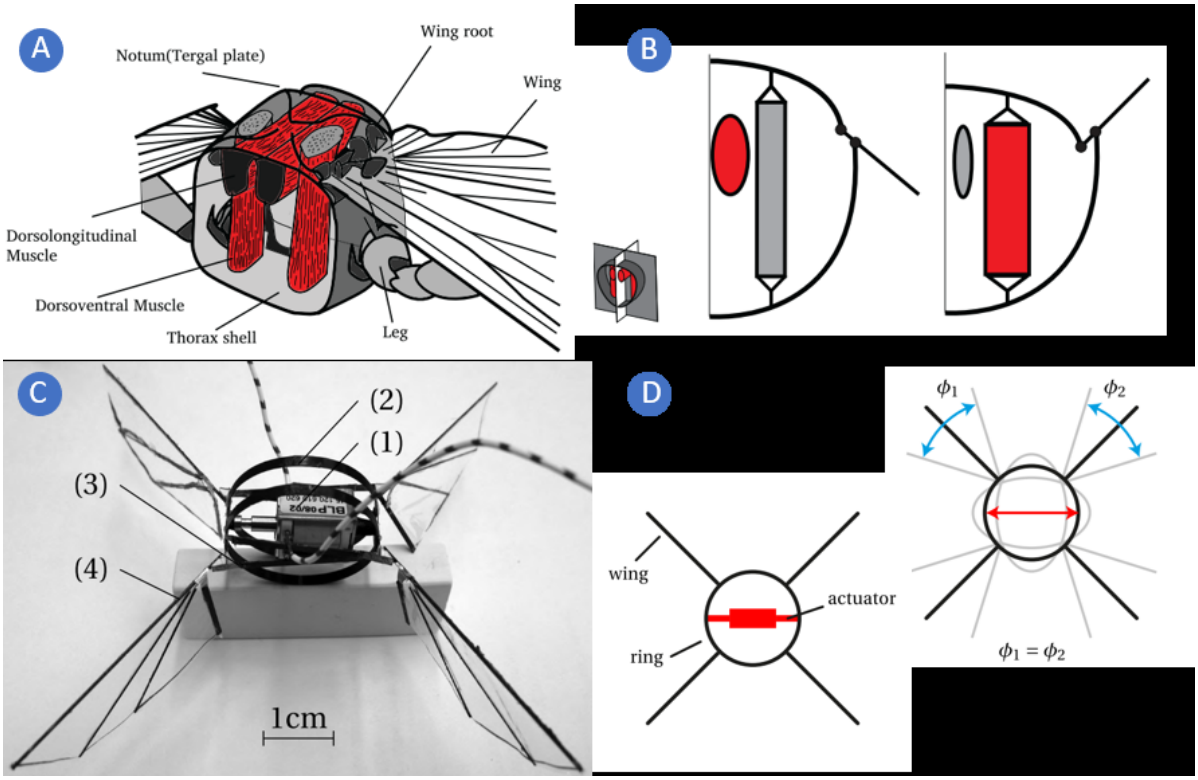


Figure 2.1: A schematic overview of the indirect flapping approach as found in insects compiled by Meindert [9]. A: Cross-section of the thorax (body) of an insect from the order of the Diptera. Several parts are labeled but the important parts are coloured red; these are the two muscle groups that deform the thorax shell which in turn drives the wings via the wing root. B: Schematic representation of the thorax shell, muscles and wings of an insect. The muscles deform the shell pushing the wing up and down. C: The Atalanta FWMAV as of 2020: (1) linear actuator, (2) deformable ring (similar to thorax shell), (3) amplification mechanism/wing driving mechanism, (4) wings. D: Simplified representation of how the Atalanta wings are actuated due to resonance of the system. Images A and B courtesy from Bolsman [7], C from Wang [32] and D from Peters [33].

### 2.2.2. Wing Design

Flapping wings at small scales generate lift based on multiple principles. Firstly, the parameters of the wings play a role; Both the geometry, as well as the kinematics affect the generated lift. Secondly, several mechanisms enhance lift generated by wings. These are the following:

- Leading Edge Vortex (LEV) - LEVs occur when the wing's angle of attack is the same as it is for stall, creating low pressure above the wing. When stall occurs the flow separates from the leading edge and reconnects further along with wing.
- Wake Capture - Wake capture occurs when the motion of the wing reverses and moves into the wake of the previous stroke. This causes the effective flow to increase.
- Clap and Fling - Clap and fling is caused by wing interaction. When moving toward eachother, the wings cause a downward momentum jet. Additionally, these interactions increase the effects of the LEVs.
- Tip Vortices - Tip vortices are vortices generated around the tip of the wing. These further enhance the LEVs.

The original wings were designed and partly optimised by Casper Bolsman [7]. A four wing design was chosen to decrease the amount of control needed for stable flight, as four wings will place the center of mass in the middle of the design in a more stable manner. Bolsman's design was capable of generating $0.9 \pm 0.05$ grams of lift while running at 27 Hz. This fell short of the required 8 g.

A more complex wing design was needed. Qi Wang designed an optimised wing in 2017. [32] Particularly, Wang optimised the shape and pitching angle of the wings. He did this by developing a quasi-steady model with four aerodynamic loading terms. This model provides an accurate prediction of the force and torque delivered by the wings. More importantly, Wang showed that an optimised twisting angle could increase the

power efficiency by up to 33% during hovering flight. Additionally, an optimised pitching angle improves the effectivenss of resonance for the wing by reducing losses at the end of a wing flap. In the next section, the hinge meant to achieve this angle is discussed. Reducing losses is an important property in resonant systems. He also concluded that a flexible wing could only outperform a rigid wing, if the rotation of the wing root is limited. Wang also suggests a flapping speed of 30 Hz. An overview of this wing optimisation can be seen in Figure 2.2.

This approach contrasts with other designs of similar size, as these usually include a straight leading edge and a quadrilateral wing.

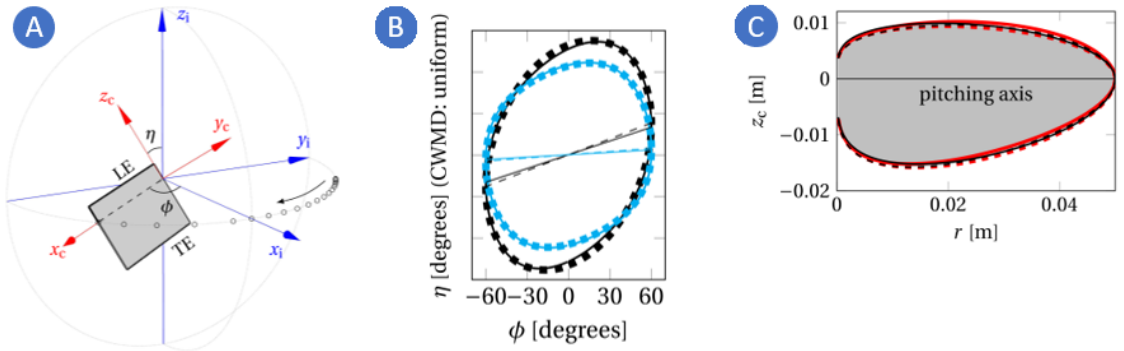


Figure 2.2: Overview of optimized Atalanta wing by Meindert [9] as developed by Wang [32]. A: wing before optimisation with its sweeping and pitching angle indicated by $\phi$ and $\eta$ respectively. 'LE' stands for leading edge, 'TE' for trailing edge. The wing pitches around the x axis of the co-rotating frame c. The pitching hinge is imaginary and located in the origin of the fixed frame i. B: Graph of the optimal kinematics of the optimized wing, expressed in the sweeping and pitching angles. C: optimized wing shape and pitching axis. Some important parameters are also listed. Note that the hinge stiffness, operating frequency, generated lift etc. are all linked. If one changes, all other parameters change. The listed values are "average" or typical values so to say.

In 2020 Meindert Ras used various methods to fabricate a set of prototype wings [9]. Ras provided a proof of concept for the results obtained by Wang and laid the groundwork for any future wings. However, the wings as produced by Ras are insufficient for sustained flight. An improved mass distribution is required and the mass needs to be reduced in order to maintain a flapping frequency of 30 Hz. Additionally, a lift-mass ratio of 0.78 was predicted, meaning either the lift of the wings needs to be increased or the weight of the actuator decreased. The approach taken by Ras differs from the usual approaching taken for the less complex wings found in other projects. These seem to prefer a sheet of mylar, or a similar material, reinforced with struts of a stiffer material. Alternatively, the power provided by the actuator could be improved.

In 2021 Abdelhakim Amer [34] performed an alternative optimisation introducing folds into the surface of a wing to remove the need for structural elements. This optimisation shows promise in reducing the mass of the wings, but requires further shape optimisations to be fabricated. Additionally, it is unknown what the performance of this wing is in its current state. It can be noted that the prototype produced is too heavy to sustain efficient flight.

### 2.2.3. Hinge Design

The hinge or wing root is the connection between the body and the wing. The bulk of research for this topic as it relates to Atalanta has been done by Meindert Ras in 2020. [9] He selected a three piece cross axis pivot hinge. This is a hinge consisting of three leaf springs arranged in a cross shape. The parameters of this hinge are dependant on the required stiffness for the passive pitching of the wing and can be calculated using Equation 2.1. The required stiffness can be determined using the optimisation done by Qi Wang. [32] This is to achieve the optimal pitching angle for the wing.

$$k = \frac{E * (2 * b) * t^3}{12 * L} \frac{Nm}{rad}. \tag{2.1}$$

Here $k$ is the hinge stiffness, $E$ is the Young's modulus, $b$ is the width of the middle flexture, $t$ is the thickness of the flextures and $L$ is the length of the flextures.

### 2.2.4. Actuators

The actuator is the main source of thrust for the Atalanta. The type of actuator greatly influences the topology and structure of the FWMAV. The main choices of actuator are either electric or chemical.

Chemical Actuators

When scaling a chemical actuator, multiple challenges arise, limiting the availability of such actuators. Firstly, due to surface-to-volume scaling, friction effects become dominant in sealing rings and cylinder walls. To avoid this, sealing rings are avoided entirely. This results in leakage and, therefore, a decrease in efficiency. [35] Secondly, heat loss can become a dominant factor when down-scaling chemical actuators. As the surface to volume ratio increases, so does the relative energy lost through the exterior of the actuator, decreasing efficiency. [36] Thirdly, a chemical engine that relies on an initial burst of energy, such as a spark-ignition engine, suffers from an effect called thermal quenching. This refers to an effect that occurs at the walls of the actuator. Here the temperature within the actuator falls below the threshold for self-sustained combustion due to losses through the exterior. At small scales this leads to a significant decrease in efficiency. [35][36] Chemical actuators also need a fuel line to deliver the reactive chemical to the actuator. The main strength of chemical actuators is the high energy density of fuels compared to electrical sources.

In 2020, Guido Mous designed a chemical actuator for the Atalanta project. [37] This actuator would allow the Atalanta 10 minutes of flight time and would weight less than 3.2 g excluding fuel source. This design requires a bellow that has yet to be developed and might become a viable solution in the future.

Electrical Actuators

Electrical actuators also experience challenges. These can be split into four main types.

- Piezoelectric
- Dielectric
- Shape memory alloy
- Electromagnetic

Piezoelectric actuators suffer from a high required voltage, which can be difficult to achieve with a carried power supply [38]. In 2020, piezoelectric actuators were used in combination with resonance to achieve successful flight [29]. As an external power supply was used, the issue of the high voltage requirement was bypassed.

Dielectric polymer actuators have a similar issue, requiring a high voltage to operate. Another issue is the slow operating speed, which could prove an issue in a 30 Hz operation [39]. A MAV was designed and fabricated in 2019. It was, however, incapable of achieving sufficient lift [27].

Similarly, shape memory alloy actuators have a low operating speed and are unlikely to be applicable for high frequency operations [40].

Lastly, there are electromagnetic actuators. These are quite ubiquitous and come in two varieties. Rotational actuator and linear actuators. As the main application for the actuator in this project will be linear, as outlined in Chapter 3, rotational actuators will require a gearbox of some design to function. This causes energy losses and increased weight for the design. The main linear solution considered will be a linear solenoid. Consisting of only two main parts and providing no resistance when not actuated.

In the prototype made by Casper Bolsman [7] in 2010, Bolsman used a linear solenoid actuator weighing 8.25 g. This actuator had a power density of 182 W/kg. In 2020, Meindert proposed the use of a linear solenoid actuator weighing 5.5 g with a power density of 145 W/kg due to the lower mass [9].

### 2.2.5. Gearbox

The use of a gearbox is not ideal for FWMAVs. It increases complexity, energy losses and weight. It can, however, lower the weight of the required actuator, in turn reducing losses and weight instead.

In 2019, a group of students investigated a linear frequency divider [41]. The intent of this divider was to double the output frequency of an actuation. The reverse might also be possible, halving the input frequency of a given actuation. This would allow double the work to be done by a linear actuator. If these frequency dividers are used in series, they could even quadruple the work done. Figure 2.3 shows a schematic of this divider. For every two strokes of x2, x1 makes one stroke. This does present the downside reducing the predictability of the system, as the position can no longer be determined by the position of the actuator alone.

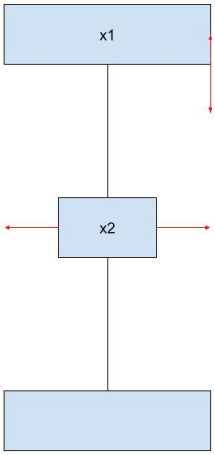


Figure 2.3: A schematic of a linear frequency divider.

### 2.2.6. Control

A lot of research has been done on the control methods for the Atalanta project as seen in Appendix A. For this research, however, this is out of scope as the main focus is on validating the flight capability of a resonant system.

### 2.2.7. Body

The body of the Atalanta acts as a spring to facilitate resonant behaviour [7], leading to a resonant frequency of the system that should be around 30 Hz. [32] This was originally realised with a simple double ring system. In 2015, N.K. Teunisse proposed a different topology using beams under torsion rather than rings. [42] An optimisation was made to refine the dimension of this new topology and it was verified using different finite element methods (FEM). This topology assists in the generation of a triangular flapping motion, a more efficient motion where the velocity is linear while speeding up and slowing down. This would require an actuator providing torque rather than a linear actuator.

Little documentation exists beyond this, however, requiring the body to be almost entirely redesigned. If a gearbox is used, sufficient integration should allow this gearbox to replace the body.

### 2.2.8. Material Selection

It is useful to determine the materials used for various components in other comparable projects. Meindert Ras [31] compiled a sizable list of information on this topic with a focus in the materials used in the wings.

Wing struts are reinforcements added to the wing to ensure the wing maintains a certain shape in flight. The most common material used for the wing struts is carbon fiber. This is a lightweight solution that retains a good stiffness property. Another material used is titanium. This solution is more than twice as dense and has a lower Young's modulus.

For the membrane constituting the surface of the wing, different materials are used. Most commonly different forms of polyester, particularly mylar. This is a material available in various thicknesses with a high tensile strength. Another material of note is kapton. Kapton seems to have poor wear resistance, but benefits from a capacity to adhere to acrylonitrile butadiene styrene, a 3D printing material. This allows struts to be printed directly onto the membrane. This would improve the production process.

### 2.2.9. Fabrication

An important facet for the creation of a prototype is the methods available to produce components. In 2019, Meinder [31] compiled fabrication methods used by other FWMAVs. Each of these has upsides and downsides unique to the method, which can be found in the following list.

- Cut and glue

  - Simple.
  - Very labour intensive.
  - Poor repeatability.

- Casting
  - Allows monolithic construction of wing, struts and hinge.
  - Suited for repeated production of identical components.
  - Suffers from deformations at small scales.

- 3D printing
  - Allows monolithic construction of wing, struts and hinge.
  - Adaptive.
  - Limited material choice.
  - Limited material predictability.

- Smart Composite Microstructures
  - Mainly useful for scales of 1 cm.

- Laser micromachining
  - Needs extra steps for a complete process.

- Heat treatment
  - Requires a seperately fabricated mold.
  - Similar to the wings made by Abdelhakim Amer [34].

Depending on the requirements imposed on a given part, different manufacturing methods may prove more advantageous than others.

## 2.3. Challenges

The completion of the design topic can be concluded to face the following challenges:

- The current fabricated version of the wings is too heavy for the used actuator to achieve the required flapping frequency. This will need to be resolved before any design becomes flight-capable as a lower flapping frequency reduces lift.
- With the lift predicted by Meindert Ras, the Atalanta is still too heavy to overcome its own weight. Either more lift needs to be produced or the actuator's weight needs to be decreased. The actuator is the biggest contributor to the overall weight.
- Very little information is available on the design of the resonant spring element. Prototype bodies have been produced and should provide guidelines for any further designs.

Each of these challenges will be addressed in the following chapters.

# 3

# Design

The following chapter lays out the requirements for a design fulfilling the design topic, followed by the design choices made at the outset of this thesis. Hereafter, the required steps for the completion of this thesis are determined and placed in order, followed by designs for the identified subsystems.

## 3.1. List of Requirements

First, it is important to outline the requirements for a design to answer the research question. This guides the design process and quantifies a condition for a failed mechanism.

1. The design has to produce a lift-mass ratio exceeding 1 when used to hover.
2. The design has to use flapping wings to generate lift.
3. The wingspan of the design must be under 15 cm.
4. The method of fabricating for the wings needs to be repeatable.

## 3.2. Design Choices

This section will discuss the options mentioned in Chapter 2 and discuss why certain options are eliminated from consideration. A full overview of the found design choices can be found in Figure 3.1. The options marked in red are eliminated and the reason why is discussed in this section. First, the broad design choices are discussed.

The control system for the design will be kept simple. It is merely meant to control the actuator into generating a 30 Hz flapping frequency. An external controller will also be used to facilitate this. With this in mind, the decision was made to also have the power supply to be kept externally, as this accelerates testing and increases the focus on the system's capacity for flight.

This leaves four systems requiring design choices. The wing (A), hinge (B), actuator (C) and body (D). The full overview of design choices can be found in Figure 3.1 and are elaborated on further below.

- A Wings
  - A1 - Folds - The optimisation for a wing design with fold rather than struts is insufficiently developed to result in a fabricated and reliable wing. It could, however, produce a wing that is significantly lighter than any alternatives. This option is chosen.
  - A2 - Struts - Ras [9] fabricated a wing using specifications from Wang [32]. The poduction method used by Ras identified some limitations that require different manufacturing methods to overcome. As such, this option is not used in favour of option A1.
- B Hinges
  - B1 - Compliant - A compliant hinge is a valid and has been investigated before. A point of note is the high frequency of the wing flaps potentially affecting the lifetime of the hinge, but this a manageable problem. A wide variety of compliant hinges exists and were evaluated by Ras [9].

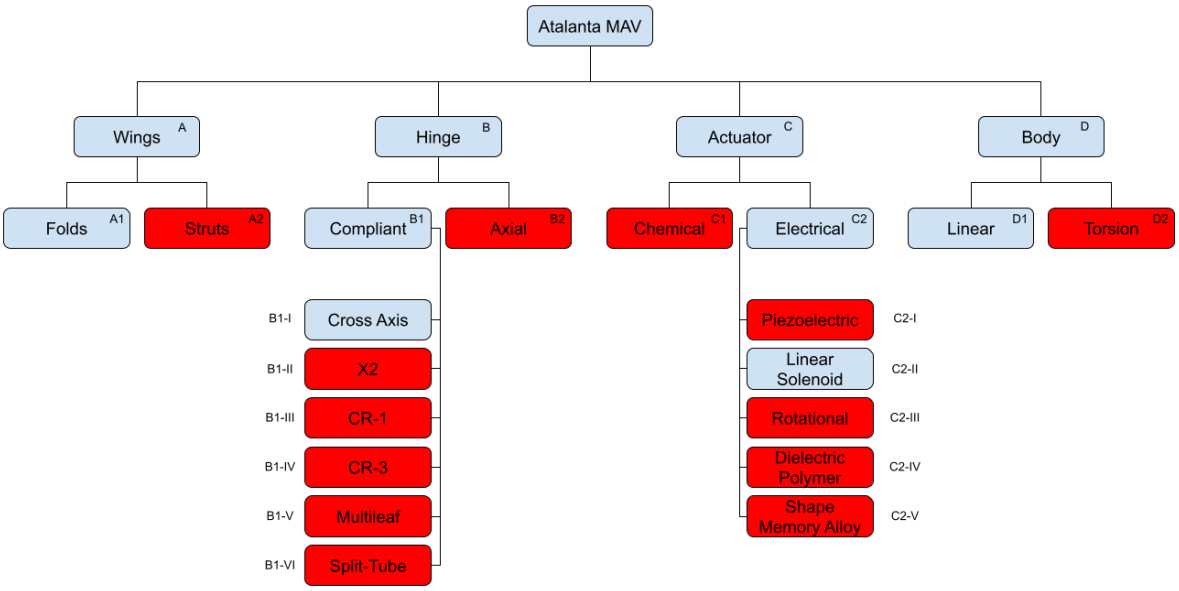


Figure 3.1: An ACCREX scheme for the Atalanta project.

- ◇ B1-I-VI - As for the selection of compliant hinges, an extensive analysis was done by Ras [9] on the applicability of various hinges. He concluded that the best usable hinge was a modified version of the cross axis hinge.

– B2 - Axial - An axial hinge is less suitable as a stiffness is desired in the rotating of the wing. This would need to be solved by adding a spring. Additionally, an axial hinge increases losses in the wing and suffers from wear. This option is eliminated.

- C Actuator

– C1 - Chemical - Chemical actuators are ruled out for two reasons. Firstly, the current state of chemical actuators is not in a producable state yet. It would cost both too much time to make and increase the risk of failing to attain flight. Secondly, an external power supply will be used in this design. This heavily diminishes the advantages given by chemical actuators as the design will not have to carry the weight of the used energy. This option is eliminated.

– C2 - Electrical - Electrical actuators normally suffer from a heavy power supply, making them less useful in a flight application. In this case, as the power supply is external, this does not become a problem. An advantage of an electrical actuator is that these are more widely available and easier to use, only requiring electricity to operate.

- ◇ C2-I - Piezoelectric actuators suffer from two problems. Firstly, a high electric field is required to create large deflections. This might not be available when the power source is carried by a drone. Secondly, piezoelectric material is usually ceramic. This means that a high frequency application such as this might shatter the material. This option is eliminated.
- ◇ C2-II - Linear solenoids are widely available. They do suffer from losses in the generated magnetic field that is not used optimally. This is the chosen option
- ◇ C2-III - Rotational electrical motors require a gearbox solution of some type, adding weight and complexity to the design, making them less desired. Additionally, this gearbox increases losses. This option is eliminated.
- ◇ C2-IV - Dielectric polymer actuators suffer two major drawbacks. Firstly, similar to piezoelectric actuators, they require a high operating voltage. Secondly, their actuation speed is slow, making it less suitable for operating at 30 Hz. This option is eliminated.
- ◇ C2-V - Shape memory alloys suffer from a slow actuation speeds, making them unsuitable for 30 Hz applications. This option is eliminated.

- D Body
  - D1 - Linear - The main advantage gained in the linear topology of the Atalanta project is the enlarged stroke it facilitates. An added benefit is that most prototypes for the Atalanta project so far have used this topology, meaning more literature is available on this design choice.
  - D2 - Torsion - Only one paper describes the principle of the torsional Atalanta topology. The idea is interesting, allowing for the use of a rotational actuator without the need for a gearbox. It lacks in two ways. Little research is directed at this way of operating the Atalanta FWMAV and no fabrication methods have been tried in available papers. The combination of these factors make the alternative far more reliable for any design. This option is eliminated.

## 3.3. Planning

In order to design the system, it is useful to determine subsystems that are mostly independent. As such, the system is divided into four subsystems: body, actuator, hinge and wing. The following list describes the constituent parts of each subsystem:

1. Actuator
2. Body
   (a) The main spring element providing the required stiffness to achieve a resonance frequency of 30 Hz.
   (b) The support structure to translate the linear motion of the actuator into a rotational stroke.
   (c) The fixture around which the wings will rotate.
   (d) The support structure transferring the motion of the actuator to the main spring element.
3. Wing
   (a) The membrane forming the thin surface area of the wing.
   (b) The struts maintaining the rigidity of the wing.
   (c) The connecting point for the hinge.
4. Hinge
   (a) A compliant element providing stiffness.
   (b) A structural element to connect the wing to the fixtures on the body.

With this overview, it can be seen that the elements fall into three groups. The hinge and the wing are interlinked and the design of one influences the design of the other. The actuator is seperate from the other elements and only depends on the topology of the body. Lastly, the body is dependant on the actuator and the hinge. As such, the body has to be designed last. An overview of the order of operations can be found in Figure 3.2.

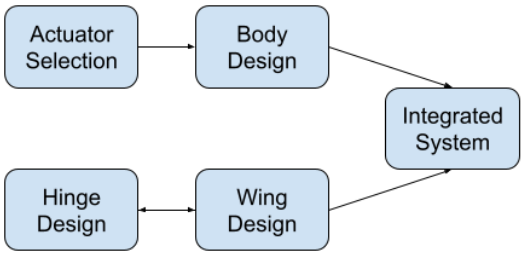


Figure 3.2: The design step order.

| | Actuator Label | Manufacturer | Mass (g) | Power (W) | Notes |
|---|---|---|---|---|---|
| A | 45-120-610-620 | PED | 8.25 | 1.5-15 | Discontinued [7], 0.0441 W vs 0.368 W |
| B | SDO-0415L | Zanty | 5.5 | 0.8-8 | [9], 0.0058 W vs 0.285 W |
| C | S1L-0211-4V | Geeplus | 1.45 | 0.67-16.67 | 0.06 W vs 0.164 W, Latching |
| D | SK-F0420 | Geeplus | 8 | 1.4 | 0.045 W vs 0.36 W |
| E | SK-A0315 | Geeplus | 5 | 2 | 0.021 W vs 0.27 W |
| F | T1L-0421 | Geeplus | 10 | 5.6 | 0.09 W vs 0.42 W, Latching |
| G | 110C | Geeplus | 7 | 2.3 | 0.082 W vs 0.33 W |
| H | H08 | Kendrion | 4.4 | 2.3 | 0.024 W vs 0.252 W |
| I | H09 | Kendrion | 4.3 | 2.3 | 0.09 W vs 0.249 W |
| J | H12 | Kendrion | 10 | 4.7 | 0.18 W vs 0.42 W |
| K | S-69-38-33 | Van Nuys | 10.8 | 4 | 0.127 W vs 0.444 W |

Table 3.1: List of linear solenoids.

The first step for designing the system is the selection of the actuator type. Depending on the type of actuator, the produced motion changes and so does the design of the body. As finding and ordering an actuator from a manufacturer can take a significant amount of time, it is important to do this first. Once this is completed, the wing and hinge can be designed in tandem. Designing both at once, slows the design process down, but allows for a better integration of the two subsystems, preventing the designs from becoming incompatible, or unnecessarily limiting the design of one due to choices made for the other. Once four wings with hinges have been constructed and tested, the body can be designed. The design can then be tested on its capacity for flight.

## 3.4. Actuator

A overview of available actuators was made as detailed in Table 3.1. The notes include the estimated power delivered and required.

Optimisation shows that the cycle-averaged power consumption for optimised wing with kinetic energy return is around 30 W/kg at 1.25 kg lift, as seen in Figure 3.3. Additionally, an optimal frequency for the wing stroke was found around 30 Hz. Additionally, a weight of 2 grams is assumed for the wings and hinges, as well as a weight of 2 grams for the body. Assuming these values, both a power delivered and requirement can be estimated for each actuator, as shown in the last column of Table 3.1. The actuators are assumed to use a mode with a duty cycle of 50%. To estimate the power provided by an actuator, the work it delivers can be calculated. The formala for work is

$$W = s * F. \tag{3.1}$$

Here s is the stroke of the actuator and F is the force delivered. This can be rewritten to find the actuators power by taking into account the operating frequency (f) of the actuator as follows:

$$P = f * s * F. \tag{3.2}$$

Effectively, this means the area under an operating graph of an actuator, multiplied by the operating frequency, indicates the power provided by an actuator.

It can be seen that the H09 and H12 actuators have some of the best characteristic among the selection. Unfortunately, these actuators proved unobtainable at lower quantities. As such, the S-69-38-33 was chosen instead, as this actuator has the third best characteristics and was already available at the TU Delft. Additionally, to get more power, a lower duty cycle can be used for a shorter amount of time. This increases the actuator's forces and, therefore, the power.

With the actuator weighing 10.8 g and the body being expected to weigh around 2 g, the wings no longer fall within the range evaluated by Wang, as seen in Figure 3.3. An optimisation needs to be run to calculate the new optimal frequency and power consumption. The used parameters for this optimisation can be found in Table 3.4 and the results can be found in Table 3.5. When all components are manufactured, a new simulation will need to be run to determine the final characteristics.

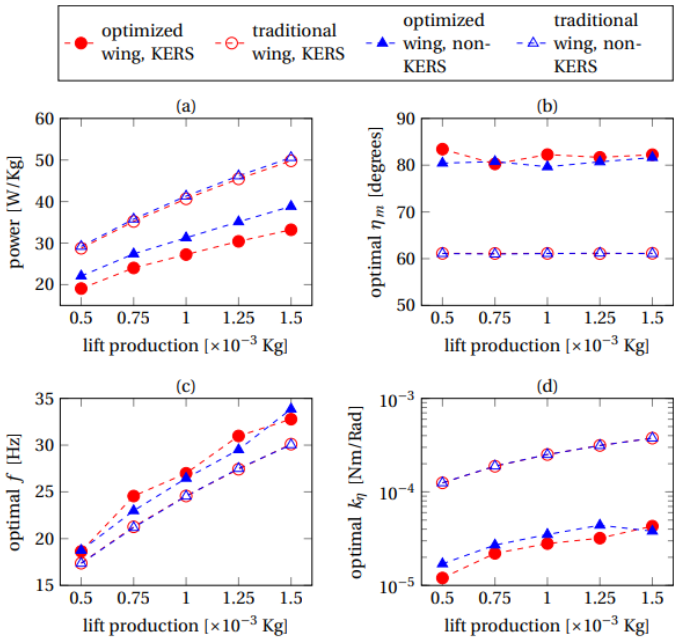


Figure 3.3: Comparison of optimal designs of the HM-wings with the kite profile CWMD for different lift constraints by Wang [32]. The HM-wings are optimized for both KERS (kinetic energy return system) and non-KERS.

## 3.5. Linear Frequency Divider

As the available actuators are incapable of providing enough power, an extra component is needed. A gearbox can increase the amount of cycles an actuators runs compared to the actuated element. Adding a gear to the chosen linear actuator would cost efficiency due to friction, as gears become less efficient with at smaller sizes. A linear solution is preferred. For this a linear frequency divider (LFD) is used. This is a frequency divider that scales the input frequency to an output frequency at a ratio of 2:1. The following section describes the design of a linear frequency divider.

The goal of a LFD stage is to allow the actuator to perform two strokes, while the actuated element only performs one. A schematic of the used LFD can be found in Figure 3.4. Here four masses ($m_b$, $m_t$, $m_1$ and $m_2$) are connected using four leaf springs ($k_l$). An actuator can be attached to $m_b$ and then connected to $m_t$. This way, when the actuator contracts, $m_1$ and $m_2$ will be pushed aside, either inward or outward. The inertia of each mass element should ensure that the masses will transition between the inner and outer position every cycle, provided the system is not critically damped. By introducing a slight offset in the springs, it can be ensured that on the first stroke, both masses move in the same direction.

The original Atalanta design [7] used a ring to cause the drone to have a certain eigenfrequency. This ring can now be replaced entirely with a LFD. For this the equations of motion need to be determined for the system to determine the eigenfrequency.

### 3.5.1. Equations of Motion

To calculate the eigenfrequency, a formula of the form

$$M\ddot{\overline{x}} + K\overline{x} = \overline{F} \tag{3.3}$$

is desired. Here M represents the mass matrix of the system and K the stiffness matrix.

Using these matrices, an eigenvalue problem can be formulated, allowing the calculation of the eigenfrequency:

$$(K - \omega^2 M)\overline{\phi} = 0. \tag{3.4}$$

The full derivation of the equations of motion can be found in appendix **??**. These result in the following mass and stiffness matrices.

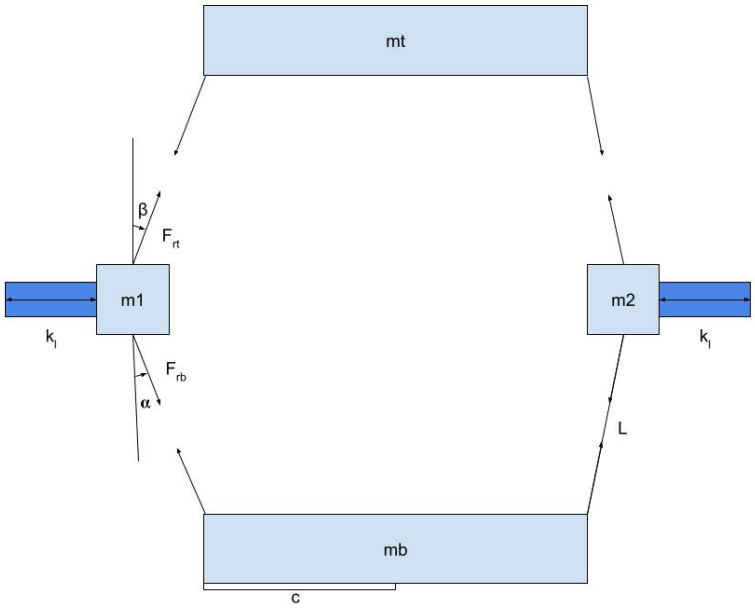


Figure 3.4: Free body diagram of a linear frequency divider.

$$M = \begin{bmatrix} 2 * m_1 - (m_b + m_t)\frac{(x_1+c)^2}{(y_1-y_b)^2} & m_a\frac{(x_1+c)}{(y_1-y_b)} \\ m_a\frac{(x_1+c)}{(y_1-y_b)} & (2 * m_1 + m_b + m_t). \end{bmatrix} \tag{3.5}$$

$$K = \begin{bmatrix} 4 * k_l & 0 \\ 0 & 0 \end{bmatrix}. \tag{3.6}$$

As the mass matrix is dependant on $x_1$ and $y_1$, the system can be concluded to be nonlinear. Using Matlab, the eigenfrequency as dependant on position can be determined. The results of this can be seen in Figure 3.5. These graphs show that the system can act linearly when operated in a certain region around zero, but, outside of this region, the system is entirely nonlinear. This means that, to determine the eigenfrequencies of the system, a frequency response function has to be generated using a numerically integrated model.

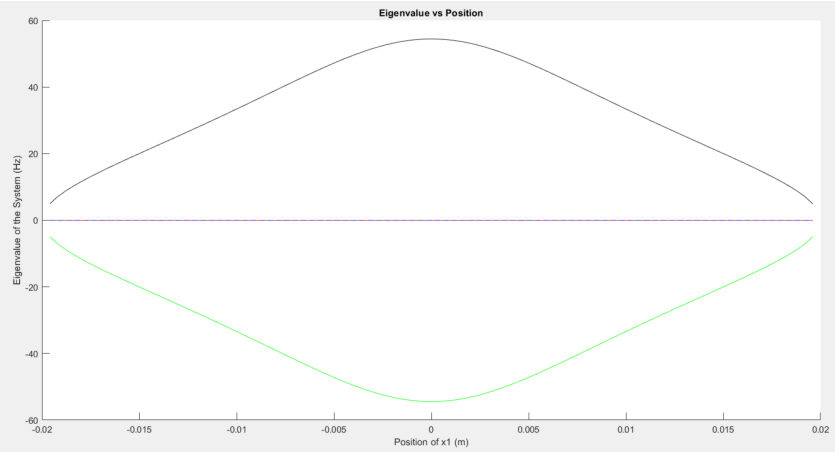


Figure 3.5: The eigenfrequency of the system as function of its position.

### 3.5.2. TMT Method

For the purpose of generating a frequency response function and gaining further insight into the behaviour of the system, a model needs to be created. Various methods of this exist. The TMT method will be chosen, as there is little interest in the reaction forces in the leaf springs and only one set of coordinates is of interest. Additionally, by using the TMT method, the elements are certain to not separate as a result of error.

The TMT method is a method of assembling equations of motion. It is referred to as the TMT method due to the fact that the mass matrtix, M, is multiplied by the transfer matrix, T, and its transposed form. The TMT method expresses all coordinates in terms of a set of generalised coordinates. This is useful if a limited amount of coordinates are of interest and the reaction forces are unimportant.

As such, a set of generalised coordinates needs to be chosen. These coordinates should be enough to describe the system in its entirety. $x_1$ and $y_1$ are chosen for this. The full script used can be found in Appendix B. It is assumed that the top and bottom mass are locked to each other and can only move closer together. It is also assumed that mass 1 and mass 2 are moving reciprocally, mirroring each other at the same height. These assumptions are represented as follows:

$$x_b = x_t = 0. \tag{3.7}$$

$$y_1 = y_2. \tag{3.8}$$

$$x_1 = -x_2. \tag{3.9}$$

The position can can then be represented as dependent on the generalised coordinates;

$$\begin{bmatrix} x_1 \\ y_1 \\ x_2 \\ y_2 \\ y_t \\ y_b \end{bmatrix} = \begin{bmatrix} x_1 \\ y_1 \\ -x1 \\ y_1 \\ y1 + \sqrt{L^2 - x_1^2} \\ y1 - \sqrt{L^2 - x_1^2} \end{bmatrix}. \tag{3.10}$$

The damping can be applied to mass 1 as it moves in the x-direction.

Additionally, a numeric method needs to be chosen to simulate the system. For this an Euler method could be used, but this can generate large errors if the step size is too small. Alternatively, a Runge-Kutte method could be used, leading to smaller errors with larger step sizes, but this method proved to be too computationally intense. The best solution is ode45 solver, as this adjusts the step size to minimise the error.

### 3.5.3. One Stage LFD

It is important to validate a model under predictable condition to confirm it is functioning as intended. For this, the values in Table 3.2 are used. These are based on the actual measurement for the first prototype as found in Section 4.1. Damping is left at 0 to evaluate the error of the system.

| Variable | Value |
|---|---|
| $m_1$ | 0.5 g |
| $m_2$ | 0.5 g |
| $m_t$ | 1.2 g |
| $m_b$ | 0.9 g |
| $k_l$ | 29.26 N/m |
| L | 20 mm |
| Damping | 0 |
| Simulation Time | 0.5 second |

Table 3.2: Values for validating the LFD model.

The system response can now be evaluated at various starting positions. For this, 0 m, 0.5L and close to L are chosen. These return the expected functions, immediately showing the systems non linearity, as the eigenfrequency is different for each graph. A minute movement can also be observed when x=0. This is a result of a small intentional deviation in the resting position of x. This prevents the system from locking should it be actuated from the x=0 position.

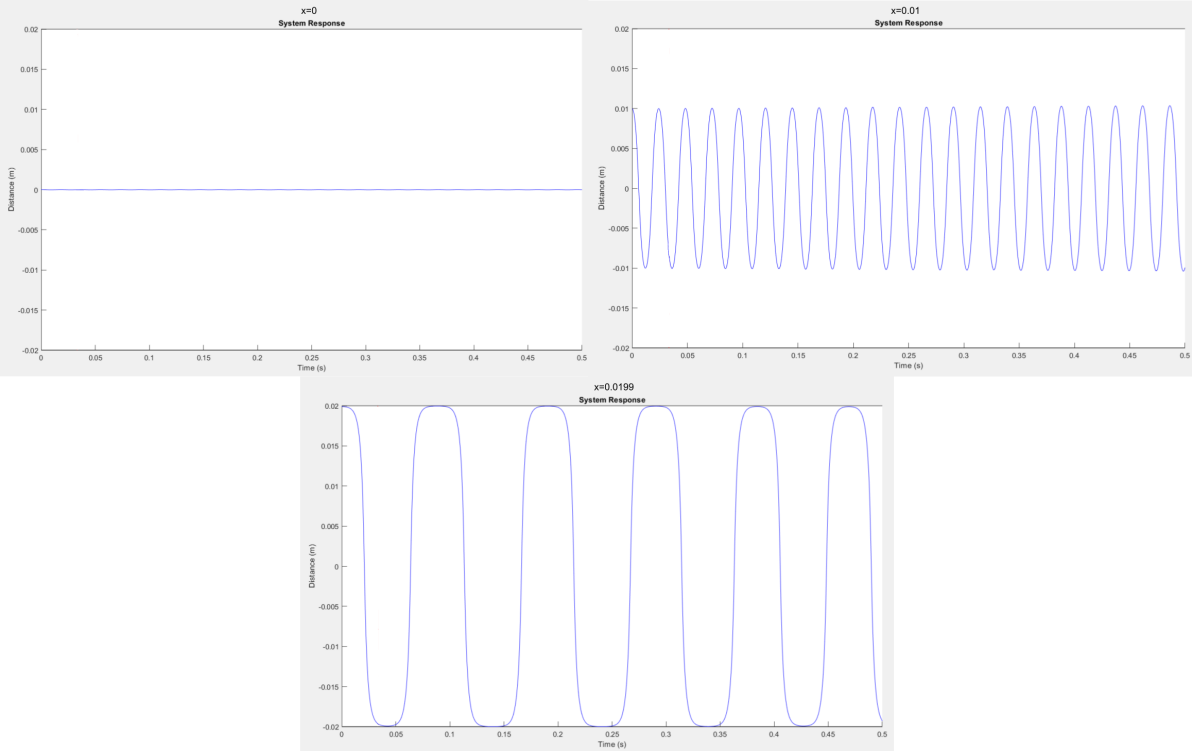


Figure 3.6: The system response of a LFD at x=0 m, x=0.01 m and x=0.0199 m.

It is now desired to have an estimate as to the actual eigenfrequencies of the system. For this Equation 3.3 can be used. The TMT element of the model and the found stiffness matrix can be used as M and K respectively. The resulting eigenfrequency can then be plotted as a function of the position $x_1$, as seen in Figure 3.5. This gives a range of frequency between which the actual eigenfrequencies can be found. For the values in Table 3.2, the highest resonant frequency is around 55 Hz and the lowest is around 5 Hz. This means that we can expect the actual lowest frequency to be above 30 Hz and the highest to be below 55 Hz.

We now put in a signal and a damping factor. The damping factor will be 0.04 and the peak force will be 1 Newton. The starting position will be set to 0.05. The simulation time will also be increased to 5 seconds. The input signal has the following form where $f$ is the frequency:

$$F_a = -F * \sin((t + 0.25/f/2) * 2 * \pi * f/2)^4 \tag{3.11}$$

As the actuator action is a pull action, $F_a$ is negative. To simulate the actuator turning off, a $\sin^4$ is used. This creates a steeper sin wave without negative values that is still continuous, unlike a step function. The input signal is left position independent for the model to reduce complexity.

It is important to remember than the goal of the LFD is to half the output frequency compared to the input. As such, any resonance frequencies found in the previous steps would need to be doubled to observe the intended operating range. In Figure 3.8 as frequency of 30, 40, 50, 60, 80 and 120 Hz are shown. It can be seen that around 40 Hz and around 80 Hz resonance occurs. Of particular note is the asymmetry present in the 40 Hz graph. The outward stroke is larger than the inward stroke. This is because the actuator is only accelerating half the motion as seen in Figure 3.9. The actuator pushes the system when it is making an outward stroke and the system resets to an inward stroke when it is off. The asymmetry can be reversed by changing x=0.01 to x=-0.01 for the initial conditions.

Finally, a frequency response function of the system can be generated. Of particular interest are the output amplitudes and the output frequencies. The phase shift is not evaluated. To observe the entire motion of interest, the frequency response function is generated from 120 Hz, generating data points every 0.5 Hz. The function is generated both starting from 0 and starting from 120. The frequency response function can be found in Figure 3.10. The output frequency is determined by dividing the number of peaks by the time elapsed. As the simulation time for each step is 120 seconds, the startup has a negligible error.

The frequency response shows two resonant regions. One is located in the desired region where the input

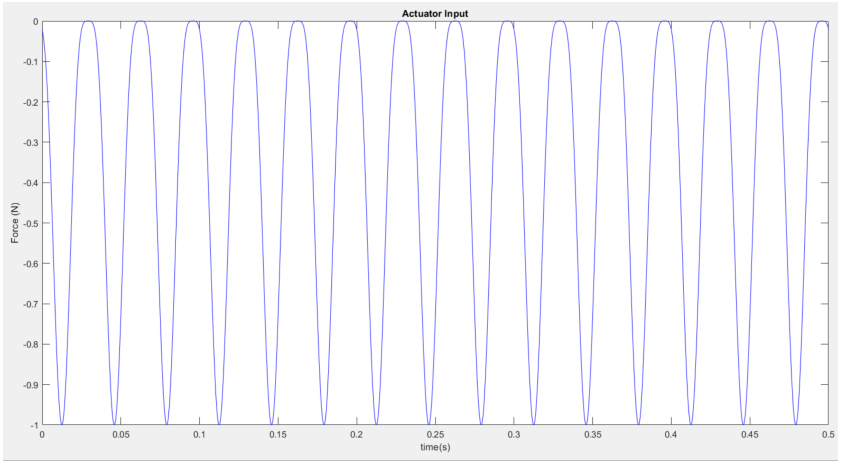


Figure 3.7: 30 Hz input signal with 1 N peaks.

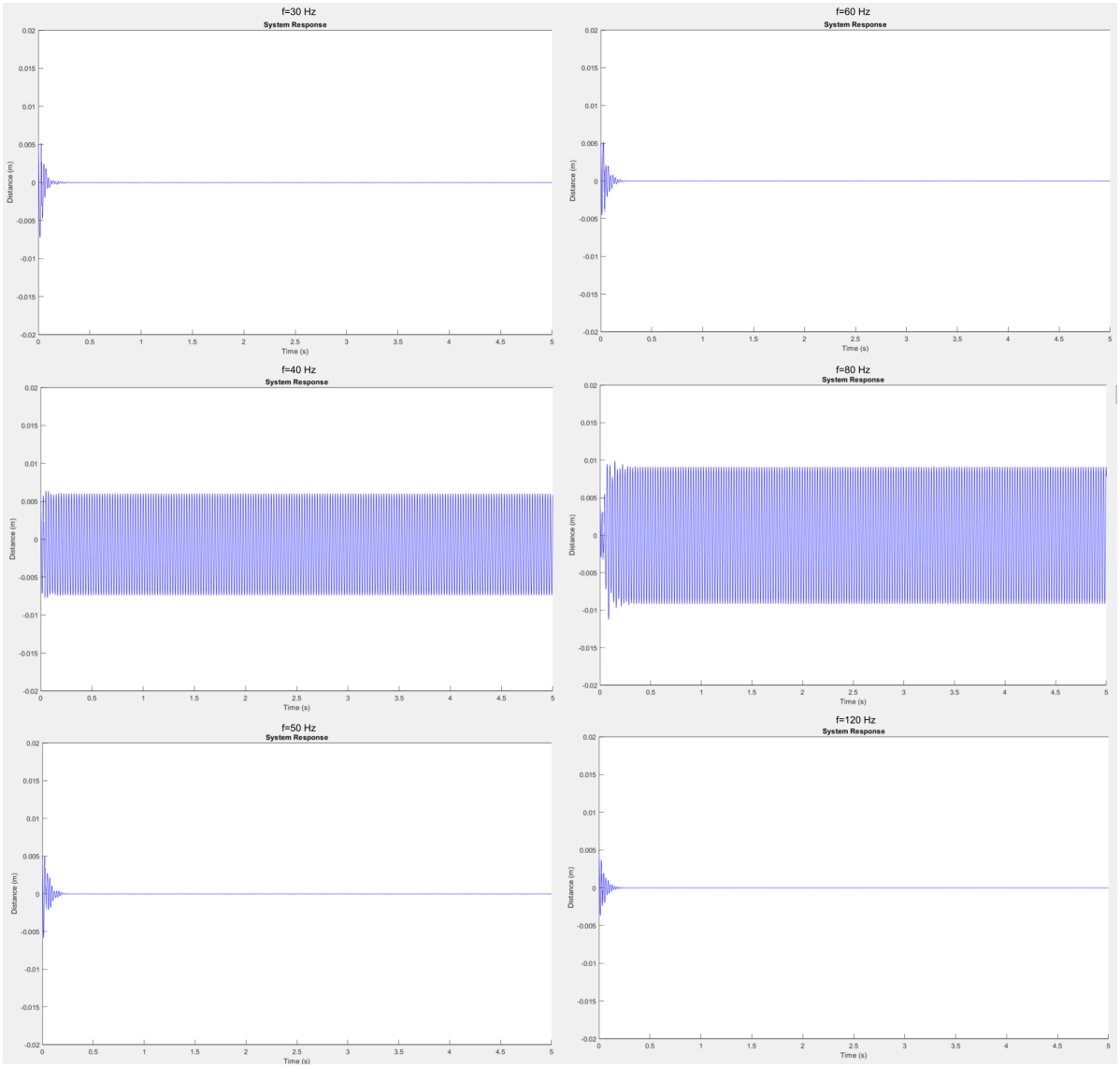


Figure 3.8: The system Response of a LFD at left: f=30 Hz, f=40 Hz and f=50 Hz. Right: f=60 Hz, f=80 Hz and f=120 Hz.

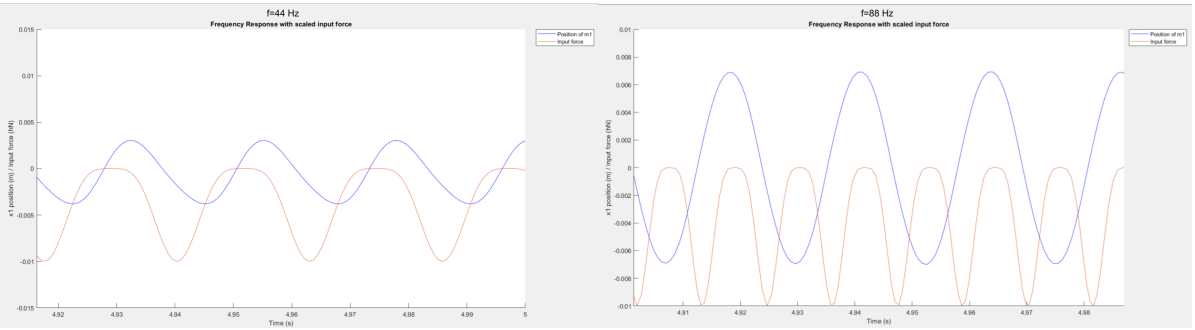


Figure 3.9: The system Response of a LFD at f=44 and f=88. Includes the input force.

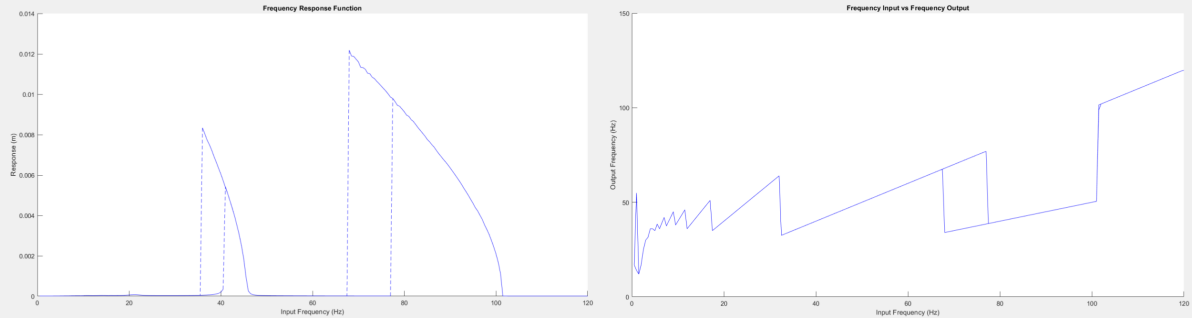


Figure 3.10: The frequency response of the system.

frequency is double the output frequency. The other is located when the input frequency matches the desired output frequency. Here the output frequency is identical to the input, rather than halved, as expected. Beyond this region, the way the output frequency is measured starts to fail, as each stroke starts to show multiple peaks.

Around 20 Hz another response can be seen. Lowering the damping the 0.02 generates the response seen in Figure 3.11. This also shows the multiple peaks per stroke mentioned before.

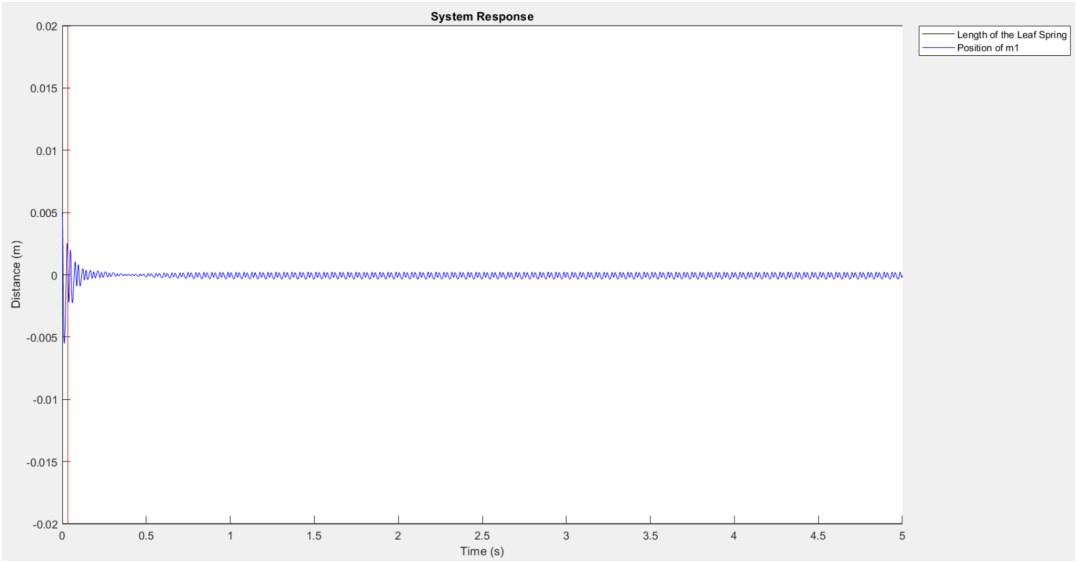


Figure 3.11: System response at f=21 Hz.

### 3.5.4. Two Stage LFD

It is possible to add a second stage to the LFD. This increases the complexity of the model greatly and introduces a pretension in the first stage. Additionally, this introduces an asymmetry in the first stage, as, when both the first stage masses are fully extended, the second stage would be centred with no tension in its springs. When both first stage masses are fully inward, the second stage would be at its greatest tension.

To model a two stage LFD, an extra set of coordinates needs to be used. Namely, the z location of the new masses. Additionally, an extra constraint needs to be added in order to relate the new masses to the old. This takes the form

$$C = (L_2 - (y_1 + pretension))^2 + (z_3)^2 - L_2^2. \tag{3.12}$$

As C is a constraint equation, the result is expected to be 0. The TMT matrix gets and extra column and row with the derivatives of C to the generalised coordinates. The Q vector gets an extra row with the time derivative of C. Due to this constraint being an element generating a force, rather than a predetermined position, like what happened with the other coordinates before, a large error can now break the simulation. As a result of this and the increased nonlinearities of the system, the complexity of this divider is greatly increased.

For this paper, the two stage LFD is not regarded, but with its potential to double an actuators maximum power a second time, could prove interesting for further study.

### 3.5.5. Modelling Wing Elements

In order to attach to the wings and have them perform a stroke, support elements need to be added to the LFD. Two hinges are required to turn the displacement of the masses into a stroke of the wing. Each hinge is also connected to one of the LFD masses.

To reduce complexity, rotation of certain elements is ignored. Due to the low mass of the parts, these rotations would have a very limited effect on the dynamics of the LFD.

A schematic of this construction can be seen in Figure 3.13. Three parts are relevant. A support element (red), connecting the furthest mass to the wing, a wing socket (green), connecting the wing to the closer mass, and the wing (yellow). The wing is directly connected to the wing socket. The wing socket is connected to the closest mass and allowed to rotated. The support element is assumed to remain straight, moving along with the furthest mass. It is also assumed to be connected to the centre of mass of the wing and wing socket. An illustration of this can be seen in Figure 3.13.

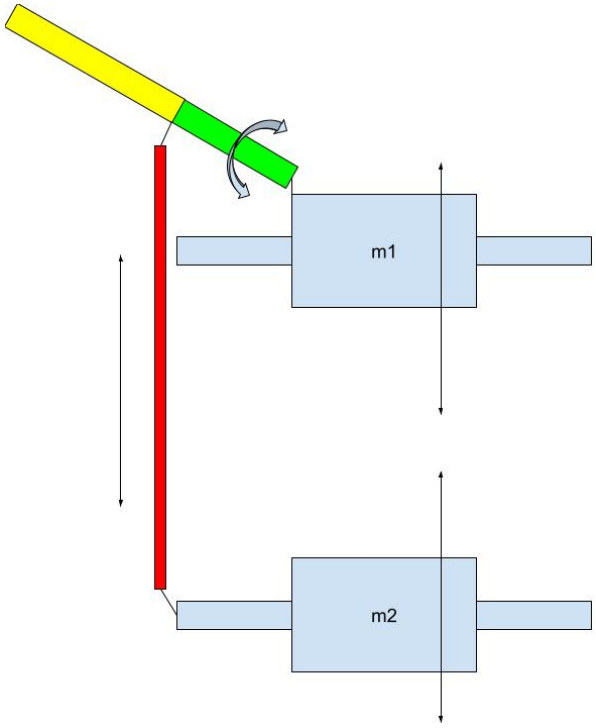


Figure 3.12: Schematic of wing connection structure. Blue: Structural masses. Red: Connecting support element. Green: Wing socket. Yellow: Wing.

Again, it is necessary to validate this model. For this the values in Table 3.3. Due to the selection of $c_p$ and $L_{\text{support}}$, the entire motion is no longer available. This is solved in the prototype by the limited range of the actuator.

| Variable | Value |
|---|---|
| Gravity | 9.81 $m/s^2$ |
| $m_1$ | 0.7 g |
| $m_2$ | 0.7 g |
| $m_t$ | 1.4 g |
| $m_b$ | 0.75 g |
| $m_{\text{w1}}$ | 0.6 g |
| $m_{\text{w2}}$ | 0.6 g |
| $m_{\text{w3}}$ | 0.6 g |
| $m_{\text{w4}}$ | 0.6 g |
| $m_c$ | 0.16 g |
| $m_{\text{socket}}$ | 0.21 g |
| $I_{\text{socket}}$ | $0.3 * 10^{-9} kgm^2$ |
| $L_{\text{socket}}$ | 2 mm |
| $k_l$ | 69.36 |
| L | 15 mm |
| $L_{\text{support}}$ | 35 mm |
| $c_p$ | 29 mm |
| Simulation time | 2 seconds |
| Damp | 0 |

Table 3.3: Properties of a generic LFD with wings.

It can been seen that the system is less stable. This can be attributed to the extra elements storing more energy than before, as well as the slight asymmetry they cause. This system's eigenfrequencies can be estimated by evaluating them as a function of the system's position, as done before. This can be seen in Figure 3.15.

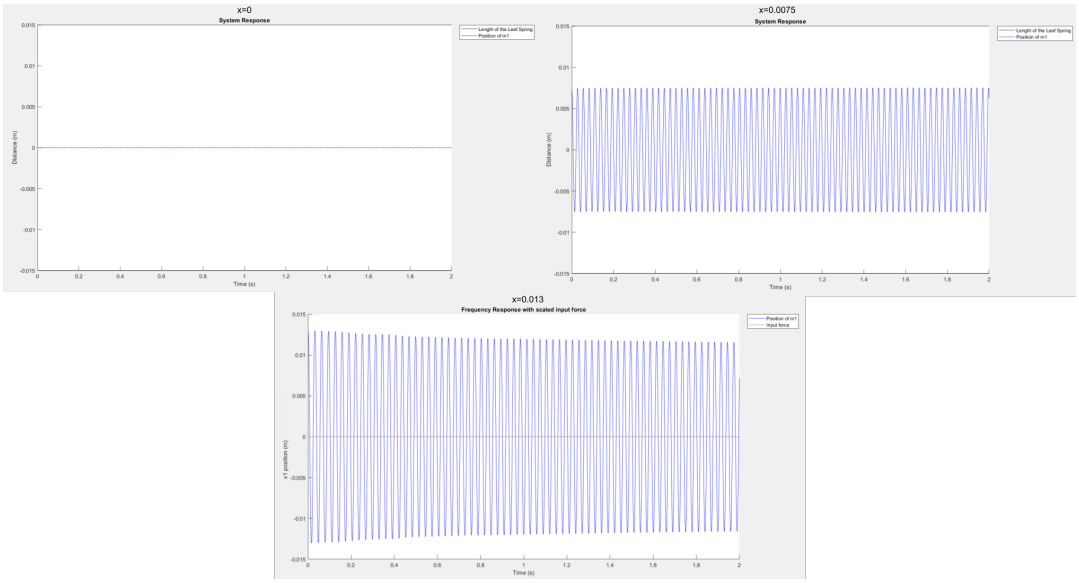


Figure 3.13: LFD with wing connectors at rest with starting position $x_1$=0, $x_1$=0.0075 and $x_1$=0.013.

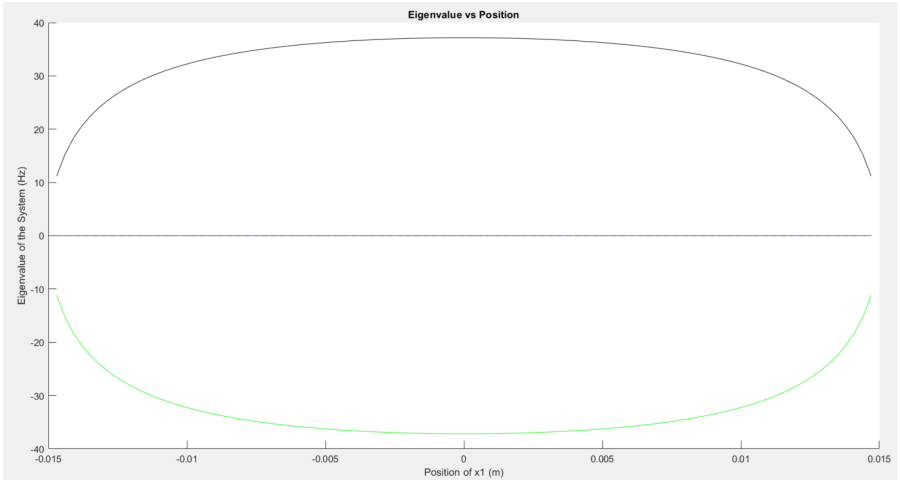


Figure 3.14: The eigenvalue of the system as function of its position

It can now be estimated that the system has an eigenfrequency below 37 Hz and above 23.5 Hz. As such, the evaluated frequencies will be f=25 Hz, f=33 Hz, f=40 Hz, f=50 Hz, f=50 Hz, f=66 Hz, and f=80 Hz. The damping used will be 0.4 and the peak force will be 1 Newton. As it is now desired to evaluate all resonant frequency, the damping factor is increased to allow the entire range of frequencies to be displayed without imaginary numbers occurring.

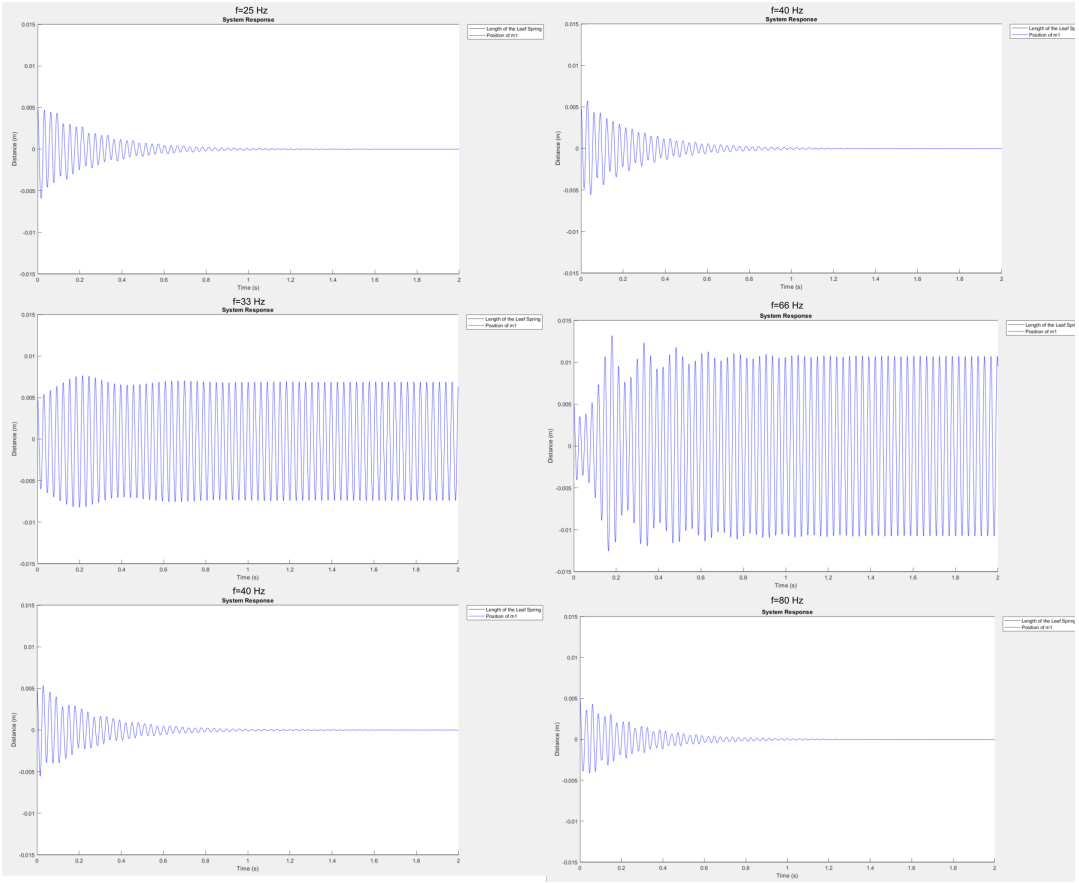


Figure 3.15: The system response of the LFD with wing connectors when exposed to a signal of: (left) 25 Hz, 33 Hz, and 40 Hz. (right) 50 Hz, 66 Hz, and 80 Hz.

For the FRF the damping factor has to be increased to 0.12. This is to prevent imaginary numbers from causing errors in the frequency response. A secondary evaluation is done using a damping factor of 0.07 at the lower frequencies, to show that the peak here still exists. The results of this can be seen in Figure 3.16. It is immediately apparent that, despite the similar masses and higher stiffness, the resonance occurs at a much lower frequency. This is to be expected, as the additional components almost double the moved masses.

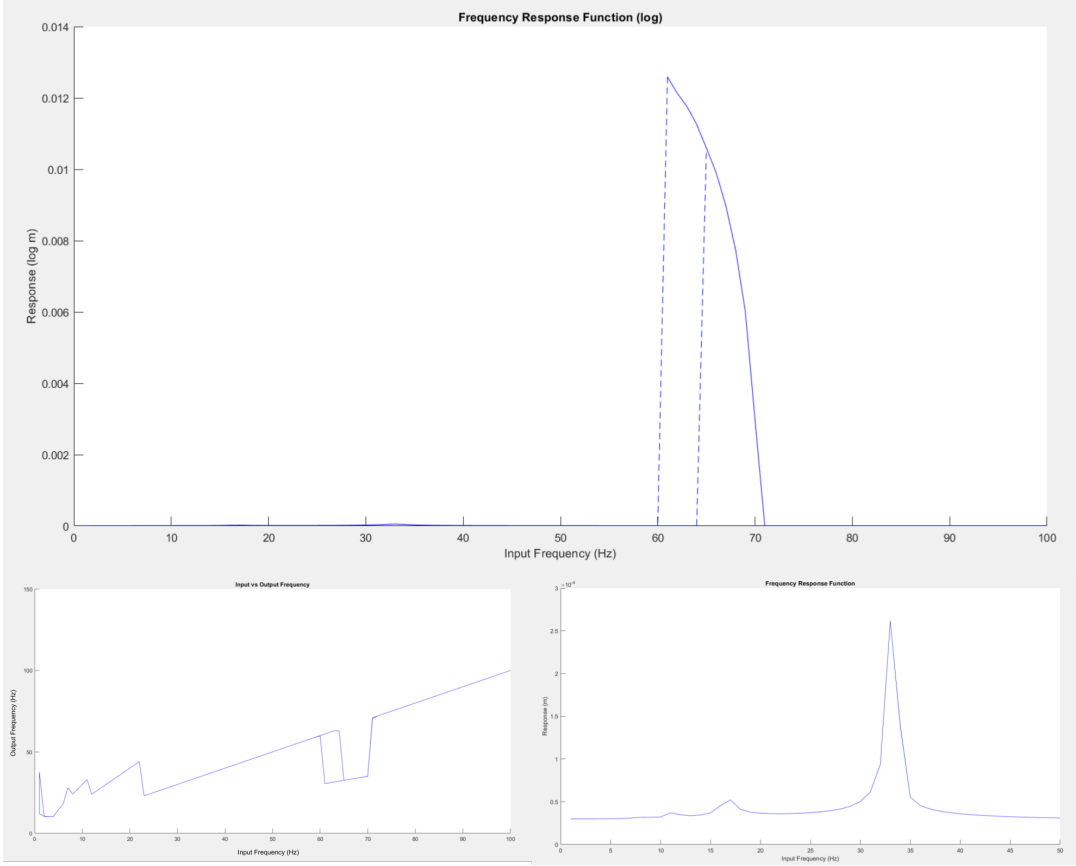


Figure 3.16: (top) The frequency response of the system with a damping factor of 0.12. (left) The frequency input vs the frequency output of the system. (right) The frequency response of the system with a damping factor of 0.07.

## 3.6. Wings

Due to the weight of the actuator, the wings are required to produce a lift of at least 14.8 grams. As mentioned before, this is outside the scope evaluated by Wang [32] and a new optimisation has to be performed. For this, the matlab scripts provided by Wang are used. As losses increase with an increased wing mass, the wing mass has to stay as low as possible. The predicted mass for the wings is set to 75 milligrams. Any increase beyond this leads to significant losses. The starting parameters can be found in Table 3.4. These parameters generated the results found in Table 3.5. The resulting wing shape can be found in Figure 3.17

| | |
|---|---|
| Number of Wings | 4 |
| Vehicle Weight | 0.0148 kg |
| Wing Mass | 7.5e-5 kg |
| Wing Length | 5 cm |

Table 3.4: Drone Parameters

| | |
|---|---|
| Frequency | 36.8 Hz |
| Losses | 39.37067 W/kg |
| Hinge Stiffness | 1.1026e-04 Nm/rad |
| Sweeping Amplitude | 1.05 rad |
| $d_t$ | 0.498835 |
| $d_r$ | 0.315868 |

Table 3.5: Wing Characteristics

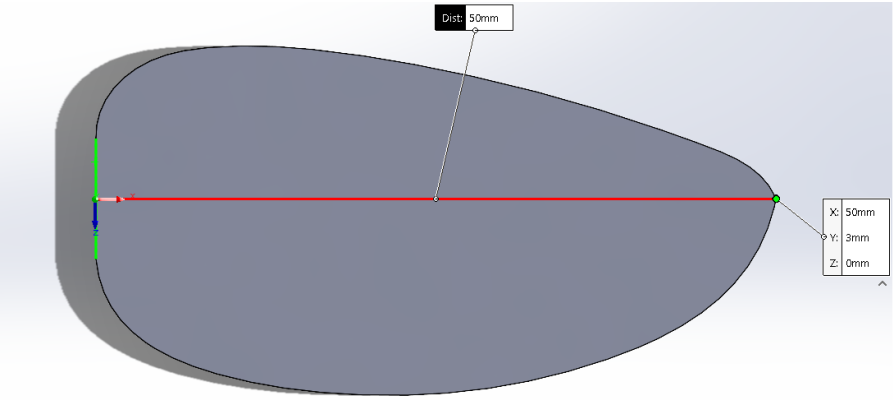


Figure 3.17: Shape of an optimised wing

Ras [9] created an overview of the Atalanta wings produced up to 2019. Since then another wing type has been produced using vacuum forming. This wing was never explicitly measured, but, using the measurements and material type provided, can be estimated to be between 150 and 300 milligrams. The only wing within the weight limit established before was the one produced by Bolsman [7], using a cut and glue method, a method that lacks precision. This implies that any method needs to add little to no material to the wings surface membrane. If vacuum forming can be used to manipulate a sufficiently thin membrane, this could be a method that is both repeatable and accurate.

### 3.6.1. Vacuum Forming

Vacuum molding is a process by which a film of plastic material can be molded to varying shapes. This is done by tensioning the plastic film over the mold and heating the plastic using a heating grill. This causes the plastic to become malleable. Once sufficiently malleable, the film is lowered to the mold and a vaccuum is applied, pulling the film over the mold where it solidifies. A mold can be made with a 3D printer.

Having modelled the wing surface in Solidworks, the total surface area is $75mm^2$ or $0.75cm^2$. Now various materials can be selected to form the wing surface. Table 3.6 lists common materials used for vacuum forming as well as mylar, a common wing membrane.

| Material | Density ($g/cm^3$) | Minimum Thickness($\mu$m) |
|---|---|---|
| Acrylonitrile Butadiene Styrene (ABS) | 1.0-1.05 | 71.4-75 |
| Acrylic – Perspex (PMMA) | 1.18 | 63.6 |
| Co-Polyester (PETG) | 1.19 | 63.0 |
| High Impact Polystyrene (HIPS) | 1.08 | 69.4 |
| Mylar (PET) | 1.38 | 54.3 |
| Polycarbonate (PC) | 1.20 | 62.5 |
| Polypropylene (PP) | 0.905 | 82.9 |
| Polyethelene (HDPE) | 0.857-0.975 | 76.9-87.5 |

Table 3.6: Common Materials for Vacuum Forming

As for the mold of the wing, it was chosen to create an iterative design. This would allow for a wide exploration of the viability and functioning of the vacuum forming process. An optimisation process would potentially lead to an improved design, but the creation of a model for this process was deemed too time intensive. With such a model, many complex and less predictable phenomenon occur. The wing is susceptible to buckling and exposed to varying loads. There is also the warping of the material to consider as a result of the vacuum molding process. As such, a process where a simple wing is slowly expanded on will prove far more effective at representing the realities of the fabricated wing.

Mylar

For the initial prototype, Mylar was chosen due to availability and low cost. It was hypothesised that, due to thinning of the material when forming, the wings would end up lighter than the chosen thickness would

suggest. As such, a sheet of 300$\mu$m and a sheet of 200$\mu$m were chosen. These would both indicate any weight reduction, as well as allowing for the stiffness of any design to be tested. The wing of 300$\mu$m weighed 0.2998$g$ after forming and the wing of 200$\mu$m weighed 0.2168$g$ after forming. This differs from the expected 0.3105$g$ and 0.2070$g$ respectively. This does imply that thicker wings benefit from some weight reduction, but, as the thinner wing is heavier than expected, could just as easily be a result of manufacturing errors. Regardless, a much thinner film is needed to produce a sufficiently light wing.

## 3.7. Hinges

For the hinge, a three piece cross axis pivot hinge was chosen, as seen in Figure 3.18. This was evaluated by Ras [9] to be the best performing hinge for the Atalanta project from among the options they evaluated. The formula used by Ras needs to be rewritten to calculate $L$ using a predetermined $b$ to correctly account for the known and unknown parameters:

$$L = \frac{2 * b * E * t^3}{12 * k} \tag{3.13}$$

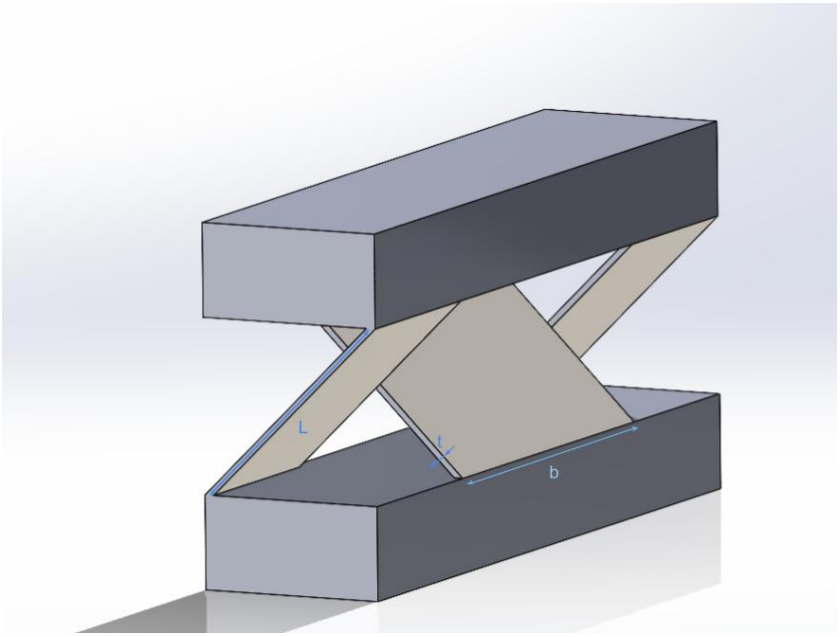


Figure 3.18: Image of a three piece cross axis pivot hinge

As a standard width of a leaf spring roll is 13 mm, 6 mm is used as the width of the largest leaf spring. The thickness ($t$) of the leaf springs is the most dominant part of the formula, however. A thickness of 0.02 mm was evaluated, but this proved to require the width of the springs to be too thin or the length of the spring too long. Ideally, the leaf springs are as short as possible, to reduce the displacement of the attached wing. The final values for the leaf springs can be found in Table 3.7.

$$L = \frac{2 * b * E * t^3}{12 * k} = \frac{2 * 0.006 * 210 * 10^9 * 0.00001^3}{12 * 1.1026 * 10^{-4}} = 0.0019\text{m}. \tag{3.14}$$

| Parameter | Value |
|---|---|
| L | 19 mm |
| t | 0.01 mm |
| b | 6 mm |
| E | $210 * 10^9$ Pa |
| k | $1.1026 * 10^{-4}$ Nm/rad |

Table 3.7: Hinge Spring Leave Parameters

# 4

# Manufacturing and Testing

The following section details the manufacturing decisions and processes used to create the Atalanta prototype. It also describes any testing setup and method used, as well as any results obtained.

## 4.1. Linear Frequency Divider

To manufacture the components for the LFD, it was chosen to use 3D printing. PLA is a relatively light weight component and the Prusa i3 MK3S is capable of forming elements accurately to around 0.5 millimeters. Additionally, the freedom this lends to the shapes of the components is useful.

The LFD can be subdivided into four distinct parts; 2 actuated masses, a top and a bottom. The function of the actuated masses is to largely determine the eigenfrequency range of the LFD. The top acts as an attachment point for the actuator core. The bottom acts as an attachment point for the actuator. For the spring elements, spring steel was chosen, as this is widely available and provides a good stiffness for its weight. Two prototypes were made to evaluate the functioning of a LFD and to validate the created model. To measure the performance of the LFD, a linear displacement sensor is used to track the position of $m_1$. The laser used was the OptoNCDT 1420LL with a 20 millimeter range. The LFD is locked in place by the base along the laser. The position of the laser can be adjusted by sliding it along a rail and locked in place by tightening the screws. This way LFDs with different spring lengths can be tested using the same setup. A schematic of this setup can be found in figure 4.2. Here the masses are marked in blue, the laser in green and the actuator in orange.

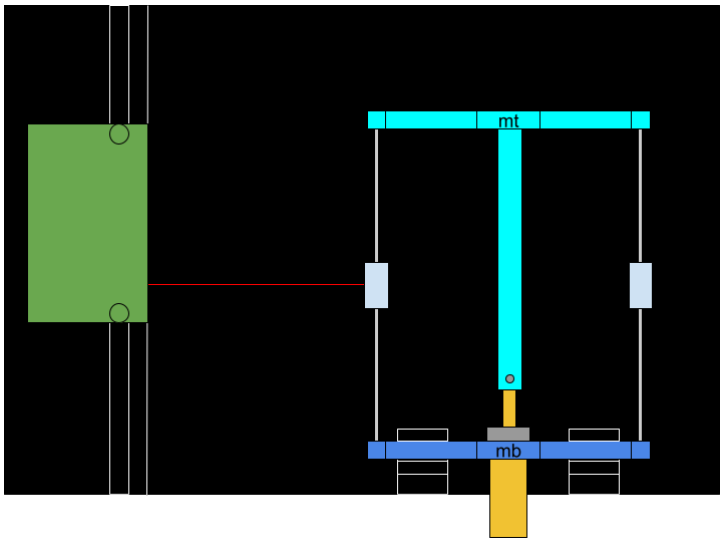


Figure 4.1: Schematic test setup for LFDs. Green: Laser sensor. Cyan: Top mass. Dark blue: Bottom mass. Light Blue: Mass 1 and 2. Grey: Leafsprings. Orange: Actuator. Black: Base plate.

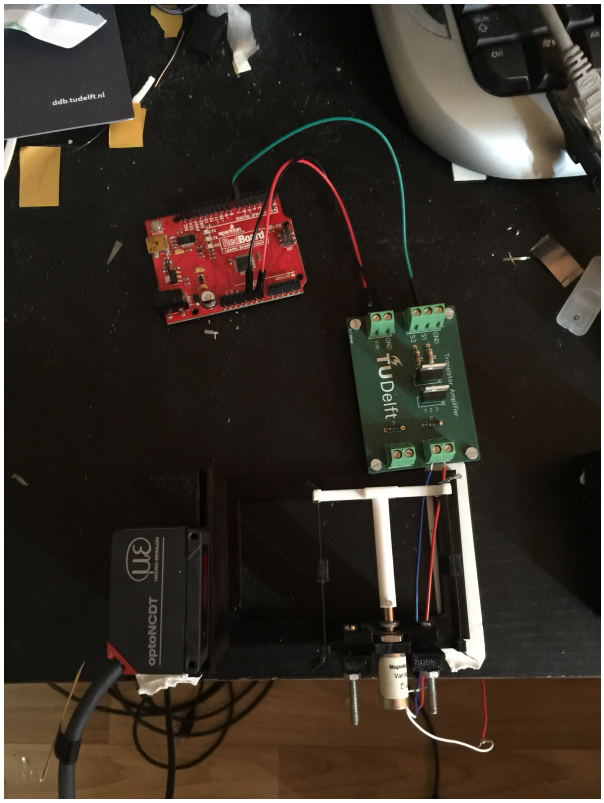


Figure 4.2: Test setup for LFDs with an Arduino Redboard and shielding circuit.

In order to aid in manufacturing, each mass has a slot with a width of 0.4 millimeter through which a leafspring can be passed. The slots on the top and bottom mass are placed at an one degree angle, to give the springs a bias outward. By bending the ends of this leaf spring, the contact area with the masses can be increased. Epoxy is then used to fix the masses along the spring. A block with the appropriate width is used to ensure the leaf springs have the appropriate length by placing it alongside the leaf spring during the gluing process. By varying the length of the beam originating from the top mass, the stroke length can be changed. If this is too large, the system will fail to move.

To actuate the actuator, some hardware is needed. As a controller an Arduino Redboard was used. Additionally, a circuit is required to protect the Redboard from the currents generated by the inductance in the linear solenoid. This circuit is drawn in Figure 4.3. To analyse the data, a matlab script was written, which modifies the measured data into a analysable format.

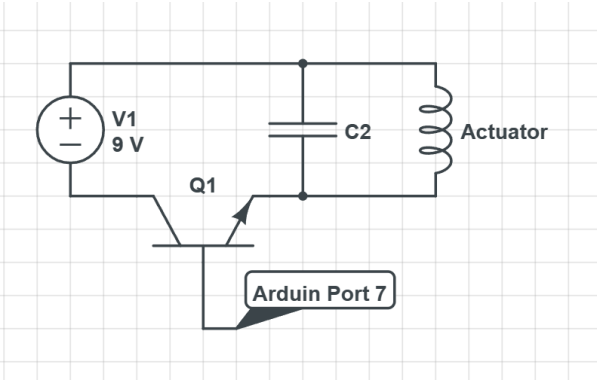


Figure 4.3: Circuit interface between the Arduino and the actuator.

### 4.1.1. Prototype 1

The first prototype was purely designed to test the frequency response of a physical version of the LFD. The actuated mass blocks are simple blocks with a slot through them. The top and bottom mass are rectangles connected by beams. The spring length for this design is 20 millimeters and the actuator stroke is around 2 millimeters. A schematic of the parts for prototype 1 can be seen in Figure 4.4.

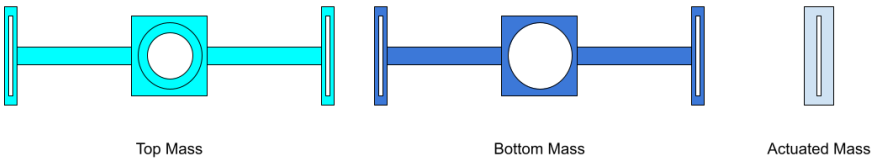


Figure 4.4: Schematic drawings of the parts for prototype 1.

The masses of the parts for the first prototype can be found Table 4.1. These can be used to generate a frequency response function. These can be compared to the measured data to see if the model matches reality.

| Part | Mass (g) |
|---|---|
| $m_1$ | 0.4715 |
| $m_2$ | 0.4756 |
| $m_t$ | 1.6087 |
| $m_b$ | 0.9335 |

Table 4.1: Mass values for prototype 1.

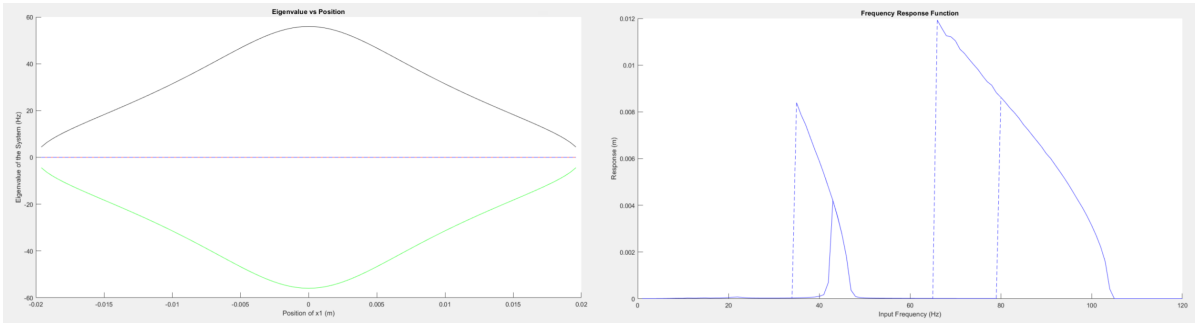


Figure 4.5: Left: Estimated eigenfrequency graph for prototype 1. Right: Frequency response function for prototype 1.

To compare these graphs to the measured data, the measured data has to be fitted to a sinusoidal graph. This is due to the measurement frequency, which is around 200 Hz. The signals that are evaluated have a frequency of 100 Hz or less. This means that per wavelength at least two data points are generated. This allows the reconstruction of the signal, which needs to happen before the output frequency and amplitude can be determined. As a first step, the startup and end of the data is removed, leaving only the theoretically sinusoidal data. To this, a sin function is fitted of the form

$$y_{\text{scale}} * \sin(t/x_{\text{scale}} + x_{\text{shift}}) - y_{\text{shift}}. \tag{4.1}$$

The fit function desired an initial guess. For the yscale it is assumed the highest measured value and lowest measured value divided by two give an accurate estimate for this value. The yshift is then the difference between that value and the highest measured position. The xscale is a result of the output frequency which can be guessed depending on which frequencies are being measured. Finally, the xshift is hard to guess accurately, as any starting value will have two potential results on the fit. As such, this is simply set to $0.5\pi$.

To confirm the quality of this fit, a root mean square error is calculated. As the graph is sinusoidal, measuring the error only vertically has limited use. As such, the distance from any measured point to the nearest point in the fit needs to be found. Additionally, the difference in time and the difference in position require

the same weight. To find the distance between the fit and the measurement the following formula can be used;

$$Error = \sqrt{x_{\text{measurement}} - x_{\text{fit}})^2 + Modifier * (t_{\text{measurement}} - t_{\text{fit}})^2}. \tag{4.2}$$

Here the modifier represent a scaling factor between the time and the position, assigning them the same weight. This is calculated by dividing double the maximum measured position by the maximum amount of time the fit can differ by. This time equals half the wavelength. This means that if a measured value is perfectly out of phase with the fit, the error of the position will be the same as the error of the time. Finally, the root mean square error is divided by the root mean square error if the error was always at a maximum. This leads to a root mean square error that can be found in Figure 4.6. In this same Figure a comparison between the fit and the measured data can also be found. If a dataset does not have sufficient high peaks, the root mean square is set to 0 instead. This might happen in section where resonance does not occur.

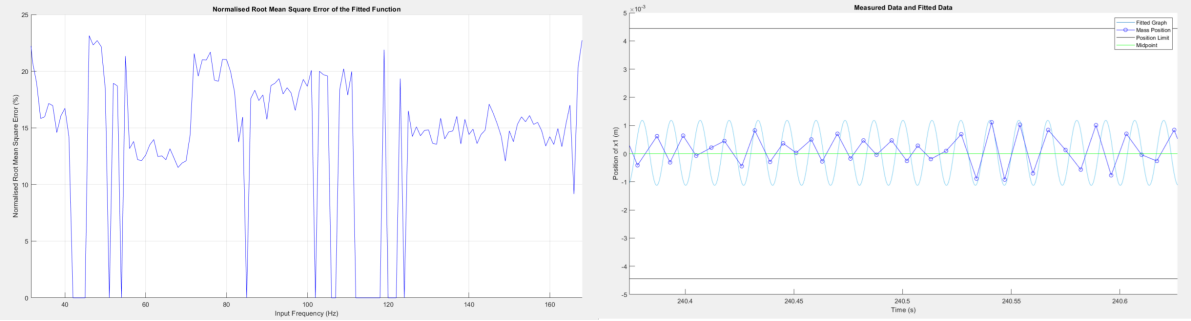


Figure 4.6: Graphs for the evaluation of the fit quality. Left: The normalised root mean square error of prototype 1. Right: The measured data of prototype 1 plotted against its fit at a random set.

The first thing of note is that the normalised root mean square error of the fit seems to be around 20%. Although this is a somewhat high value, comparing it to a line plotted through 0, which has a root mean square between 30% and 50%, it can be concluded that this is not an unreasonable fit. Looking at the measured data, it can be seen that, for certain sections, the data follows the fit perfectly. After and before these section the data will misalign for a short duration before aligning again. This could be an indication of the frequency of the fit and the frequency of the measurement being mismatched. This does not explain, however, how quickly the data returns to aligning with the fit. A better explanation is that this result is caused by noise resulting from buffering. This would occur due to data being requested by the monitoring computer, but being received at a delay. This results in an erroneous timestamp being attributed to certain data. This would also explain the relatively high root mean square error if the fit is correct. Keeping this in mind, the fit is deemed sufficient to draw needed conclusions off of.

In Figure 4.7, the measured data of prototype 1 can be seen. The first thing of note is the presence of all three predicted resonance regions. Secondly, the assymmetry predicted in the second set of resonance frequency is clearly present. Lastly, the resonance frequencies do seem to double or half as expected. What is not expected is the frequencies where these resonances occur and the amplitude they have. It is expected, as the damping in the system is low, that the amplitude of the resonance frequencies increases to the maximum attainable value. This seems to only happen in the first half of the second set, however. Additionally, the lowest frequency of the second set, does not have a counterpart in the third set. The highest frequency of the second set, when doubled, does equal the highest value of the third set, however. With these factors in mind, it can be concluded that an unforeseen resonance is occurring around 60 Hz. This, as well as the other two phenomenon will be expanded on in Section 4.1.2. The weight of the springs and glue is not sufficiently significant to cause the error in resonance frequency. Even if it were, the increase in weight would lower, rather than increase, the frequency. This leaves the conclusion that the difference in resonance frequency is caused by an increase in spring stiffness. This could be caused by the manufacturing method coating the springs in a layer of epoxy. It is possible to conclude that the output frequency is half that of the input in the operating area, even if this is at a higher than expected frequency, as such, doubling the work done by the actuator.

Q-factor

Of interest is also the Q-factor of the prototype, the formula for which can be found in Equation 4.3. By giving the system a single, prolonged activation, applying the actuator for a full second, the damping effects can be

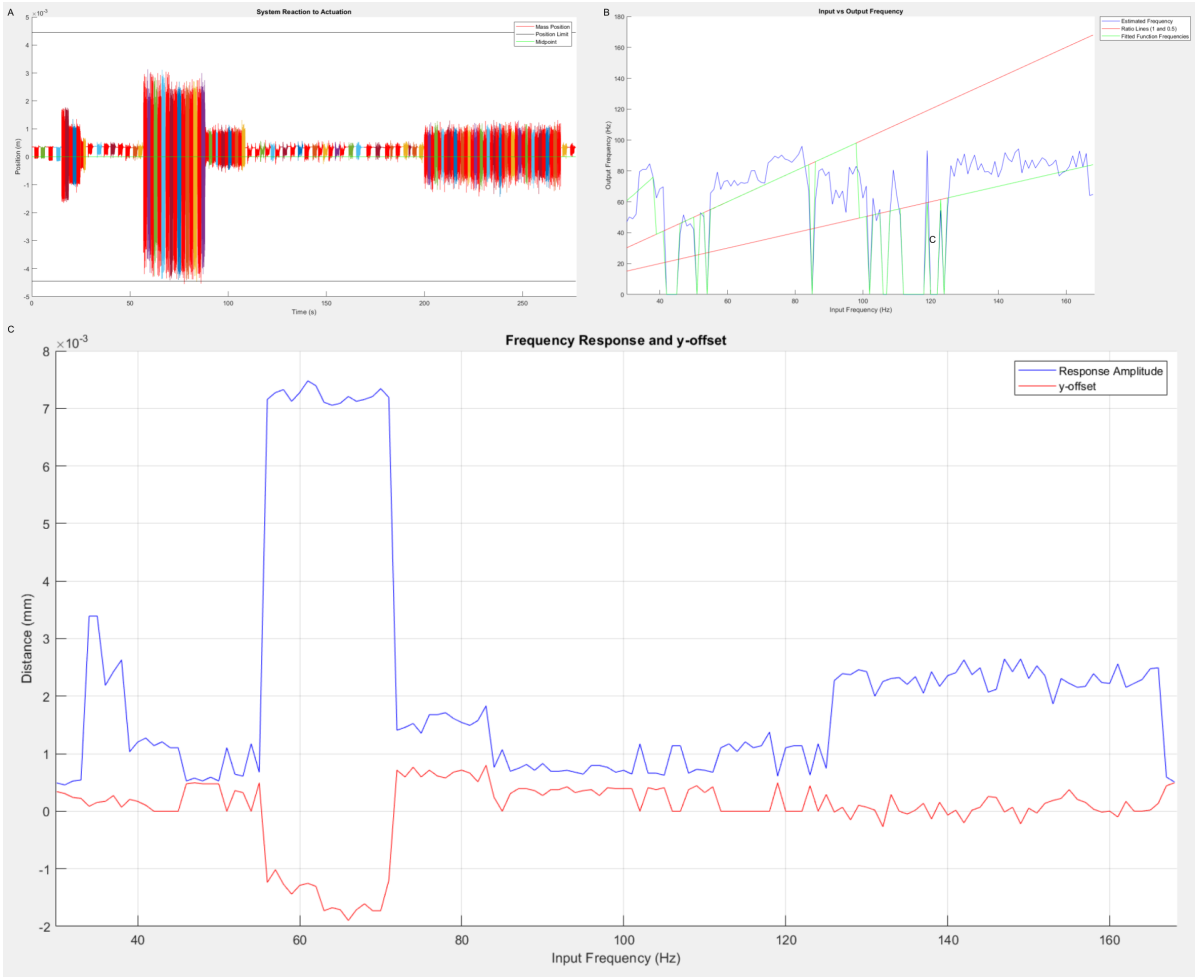


Figure 4.7: Graphs showing the measured data of prototype 1. A: The measured data of prototype 1. Each colour change has data from a different frequency. B: The estimated and fitted frequencies vs the input frequencies. The red lines indicates a input to output ratio of 1:1 and 2:1. The blue line is an estimate of the ouput frequency based on the data. The green line is the ouput frequency as found by the data fit. C: The measured peak data and offset.

observed. By comparing the peaks and, therefore, the energy stored in the system by the springs alone. As the springs do not change as a consequence of the position and the springs remain the same, these elements can be eliminated when dividing to find the Q factor. This leaves the position squared as the parameter of interest taking the following form;

$$Q = 2\pi * \frac{\text{Energy stored}}{\text{Energy dissipated per cycle}}, \tag{4.3}$$

resulting in

$$Q = 2\pi * \frac{x_1^2 \text{at t=0}}{x_1^2 \text{at the first peak}}. \tag{4.4}$$

In Figure 4.8 it can be seen that the system has a high Q-factor. Due to the sample rate, some data points are missing and this graph cannot be fit to any standard form due to the changing frequency. An estimate can be made, however. Looking at the latter half of the graph, a starting value of 12.76 is found. Then, by taking the next value at the lowest valley 12.83 is found. Finally, by looking at the start of the graph, a zero position can be found and is 12.99. As such,

$$Q = 2\pi * \frac{(12.99 - 12.76)^2}{(12.99 - 12.76)^2 - (12.99 - 12.83)^2} = 12.2. \tag{4.5}$$

As this value is higher than 0.5, it can be concluded that this system is underdamped. It is important to note that this value is a lower estimate.

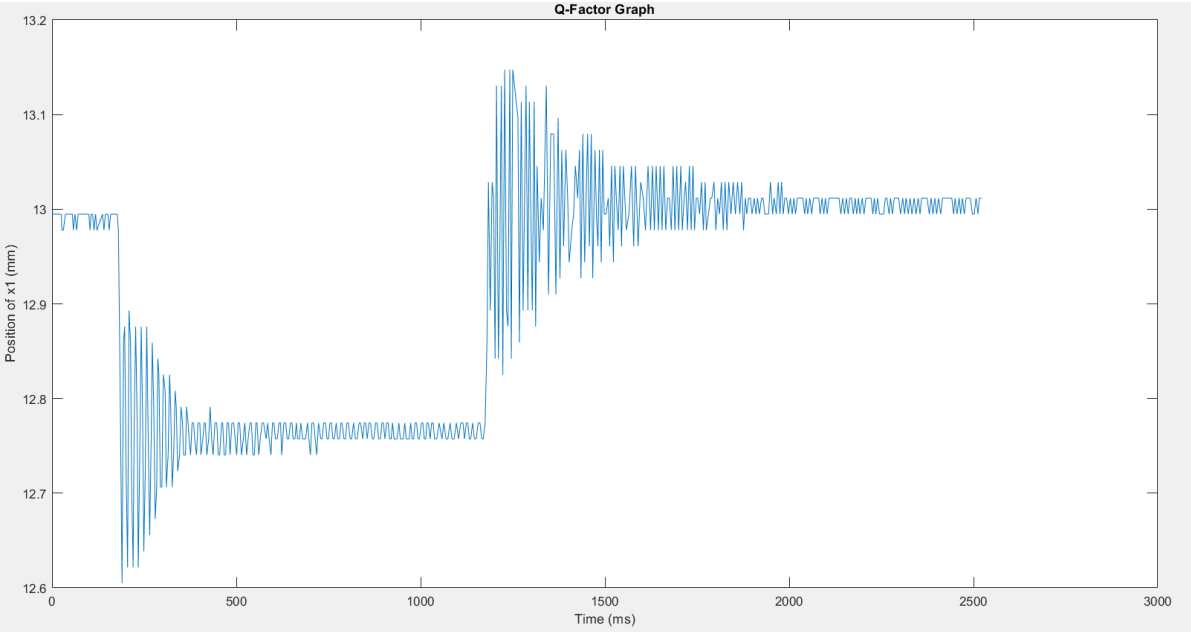


Figure 4.8: Prototype 1's response to an prolonged actuator activation.

### 4.1.2. Prototype 2

The second prototype was intended to test the design when it includes the elements connecting the wings. This design also reduced on the weights of the top and bottom mass, by removing unneeded volume. Schematics of these parts can be found in Figure 4.9. The parameters for these parts can be found in Table 4.2. Here $m_{\text{wc1}}$ refers to a support element and $m_{\text{ws1}}$ refers to a wing socket. The springs are chosen at 15 millimeters, to set the predicted eigenfrequency slightly below the desired, following the observations of prototype 1. The position of the masses was then measured.

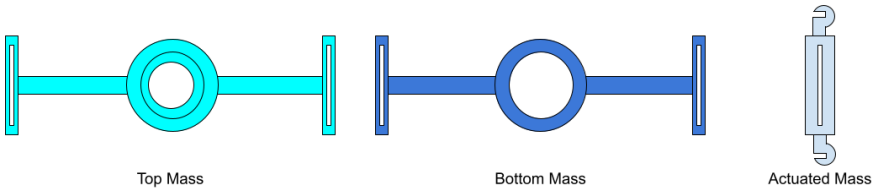


Figure 4.9: Schematic drawings of the parts for prototype 2.

| Part | Mass (g) |
|---|---|
| $m_1$ | 0.6807 |
| $m_2$ | 0.6814 |
| $m_t$ | 1.3632 |
| $m_b$ | 0.7661 |
| $m_{\text{ws1}}$ | 0.2123 |
| $m_{\text{ws2}}$ | 0.2128 |
| $m_{\text{ws3}}$ | 0.2124 |
| $m_{\text{ws4}}$ | 0.2135 |
| $m_{\text{wc1}}$ | 0.1412 |
| $m_{\text{wc2}}$ | 0.1407 |
| $m_{\text{wc3}}$ | 0.1405 |
| $m_{\text{wc4}}$ | 0.1405 |

Table 4.2: Mass values for prototype 2.

Using those masses, the predicted eigenfrequencies can be found and are plotted in Figure 4.10.

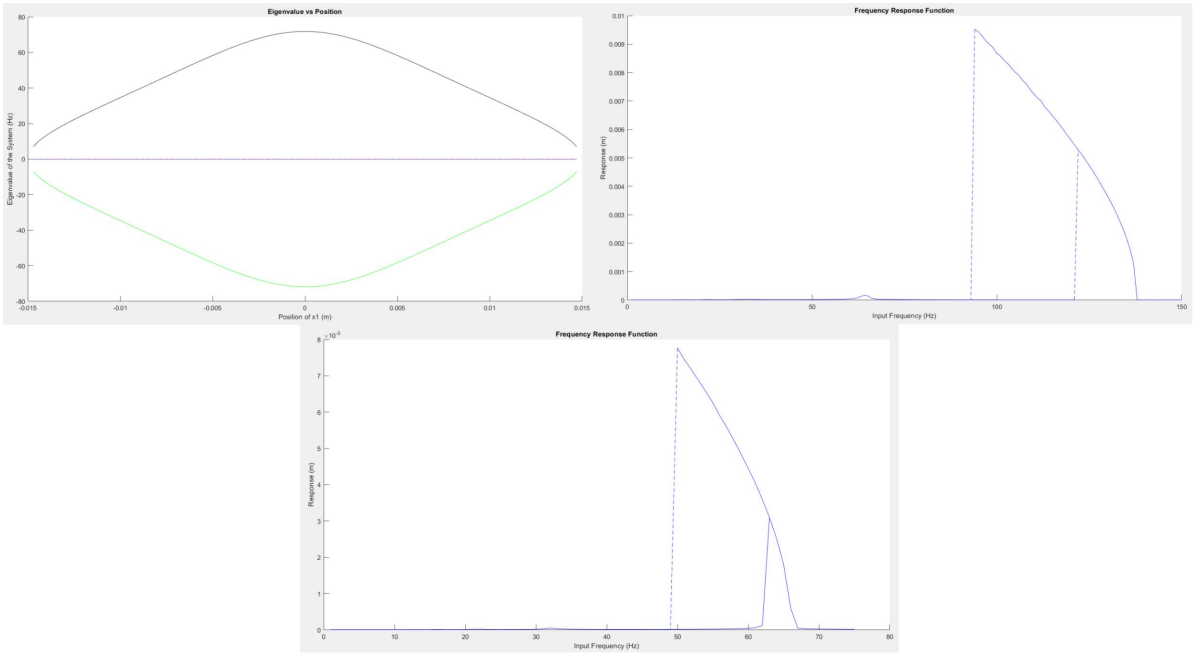


Figure 4.10: Frequency response function of prototype 2 without wing connection elements.

As described in Section 4.1.1, the measurement data of prototype two was adjusted to allow for elvaluation. During testing, an assymetry between the two masses was observed, warranting two measurements to be made, one for each mass. As the springs in prototype 2 are shorter, any manufacturing error becomes more pronounced. The measured data as well as the normalised mean square error can be found in Figure 4.11. Like in prototype 1, the frequencies are shifted to be higher than predicted. Additionally, three sets of resonant frequencies can be seen. Finally, the second set contains asymmetric data, like expected. It can also be seen that the fit is similarly accurate as when it was used on prototype 1.

Finally, the amplitude and offset of the measured data can be observed as seen in Figure 4.12. Again, it is observed that the mechanism does not move to the furthest possible position like expected. As the resonant frequencies between the two masses are different. Mass 1 (top) starts resonating around 85 Hz and stops around 62 Hz. Mass 2 (bottom) starts resonating around 75 Hz and stops around 52 Hz. When both masses are resonating, a significant increase in amplitude is observed. It can also be seen that, once a mass falls below its resonant frequencies, it interferes with the resonance of the other mass. This can be seen the graphs of mass two below 62 Hz. Additionally, resonance frequencies below 62 Hz do not have a corresponding frequency in the third set. As such, it is concluded that the frequencies of the third set correspond to the highest and lowest resonance frequency of the stiffest spring. It also seems that the amplitude of the position measurement is affected by a similar effect. Lastly, an offset can be observed in the data of the third set of mass 1. As this offset corresponds to an increase in amplitude, however, it is likely to be the result of a measurement or manufacturing error. This offset seems to correspond to the resting position of the spring.

Having measured the characteristics of prototype 2, the connectors are now added, but not the wings. At damping 0.05 and 0.03 this gives the graphs in Figure 4.13, predicting the eigenfrequencies of the new system.

Actuating the prototype, no significant movement is observed. Instead, the Q-factor of this prototype is determined and is,

$$Q = 2\pi * \frac{(14.03 - 13.79)^2}{(14.03 - 13.79)^2 - (14.03 - 13.88)^2} = 10.3. \tag{4.6}$$

This is significantly lower than the,

$$Q = 2\pi * \frac{(14.20 - 13.89)^2}{(14.20 - 13.89)^2 - (14.20 - 13.96)^2} = 15.68, \tag{4.7}$$

of the prototype without the wing elements. It can also be observed that more force is required to move the prototype into the same position, as the end position of the adjusted prototype is 13.95, oppose to 13.6. As

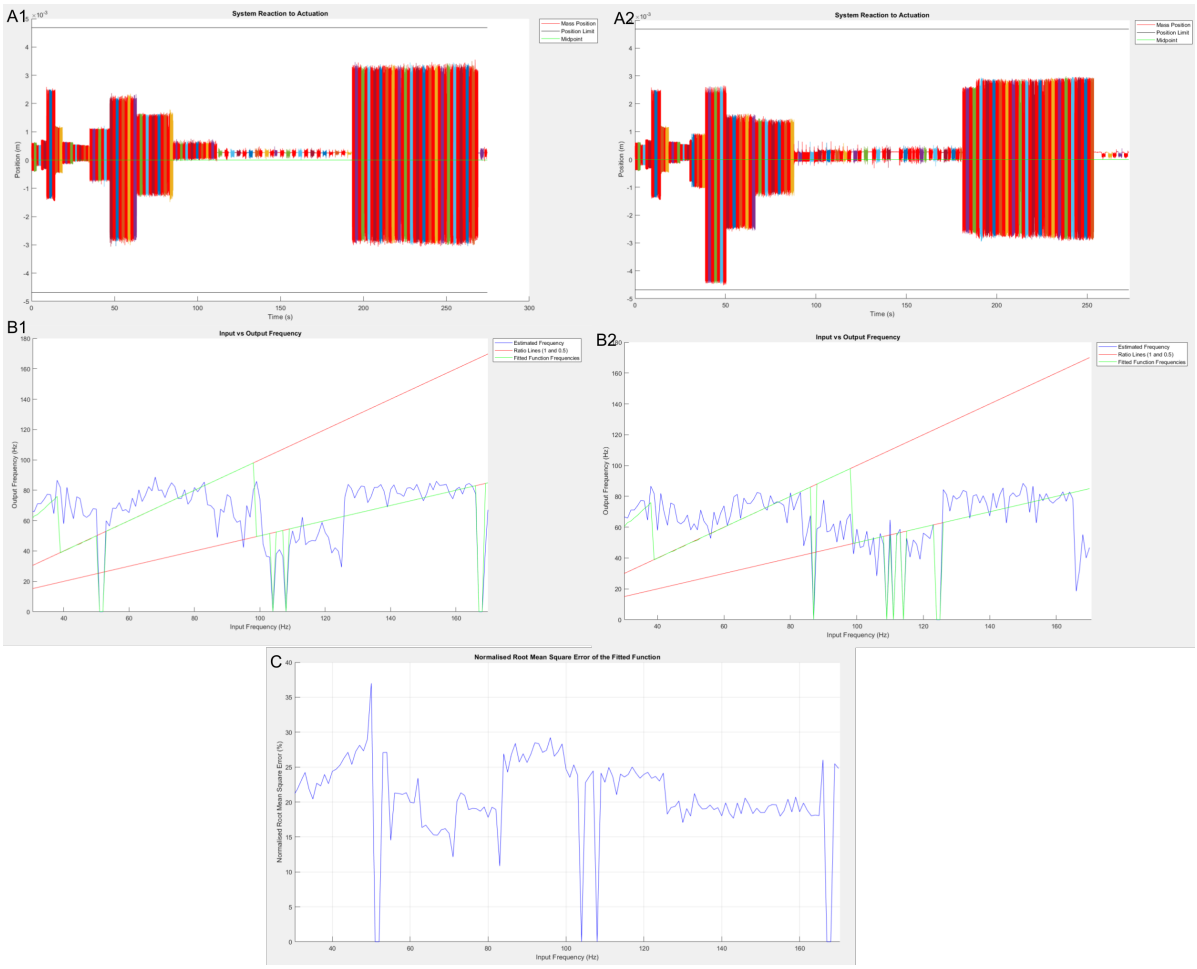


Figure 4.11: Prototype 2's measured data. 1: Mass 1. 2: Mass 2. A: Measured position data. Each colour change indicates a change in input frequency. B: The estimated and fitted frequencies vs the input frequencies. The red lines indicates a input to output ratio of 1:1 and 2:1. The blue line is an estimate of the ouput frequency based on the data. The green line is the output frequency as found by the data fit. C: Normalised root mean square error.

such, it is possible that a more powerful actuation could get the system to properly resonate. It was measure that around 101 Hz, the system responded marginally more, but no meaningful measurement can be taken. As such, the flight test cannot be performed with this prototype.

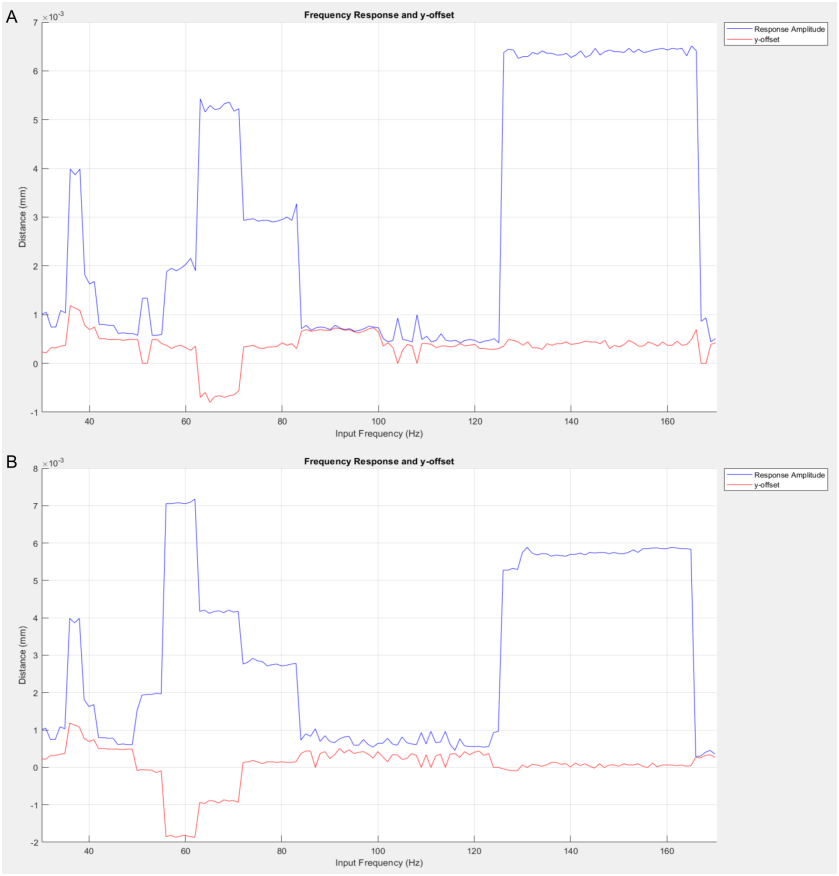


Figure 4.12: Prototype 2's amplitude data. A: Amplitude data of mass 1. B: Amplitude data of mass 2.

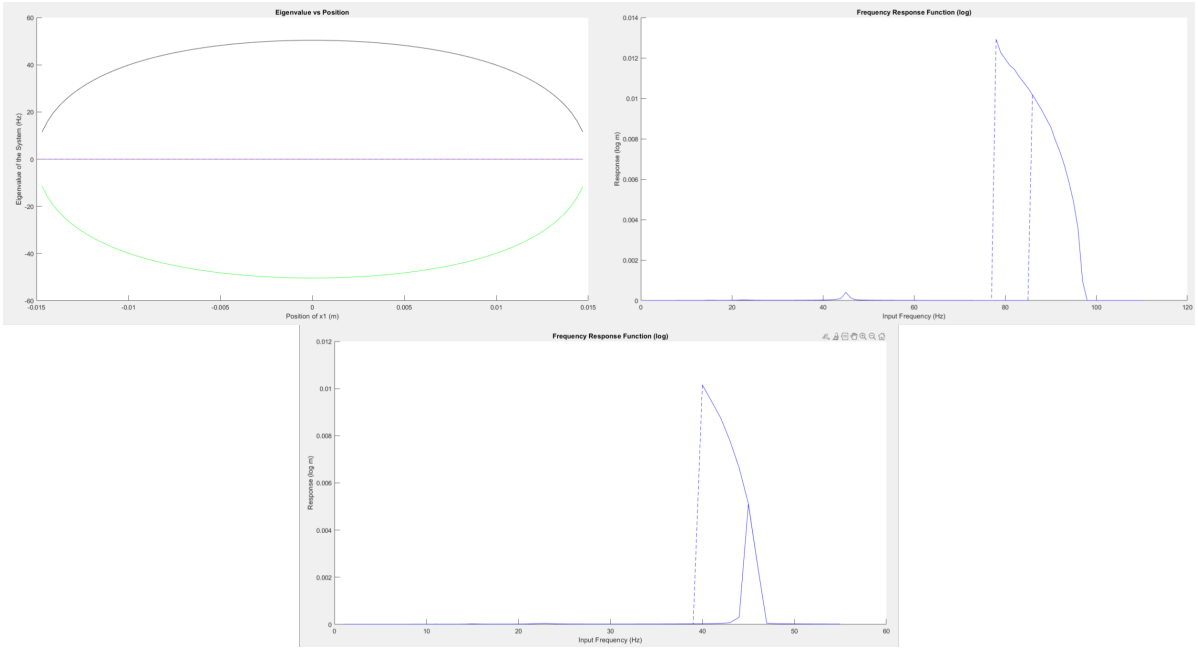


Figure 4.13: Frequency response function of prototype 2 with wing connection elements, but without wings.

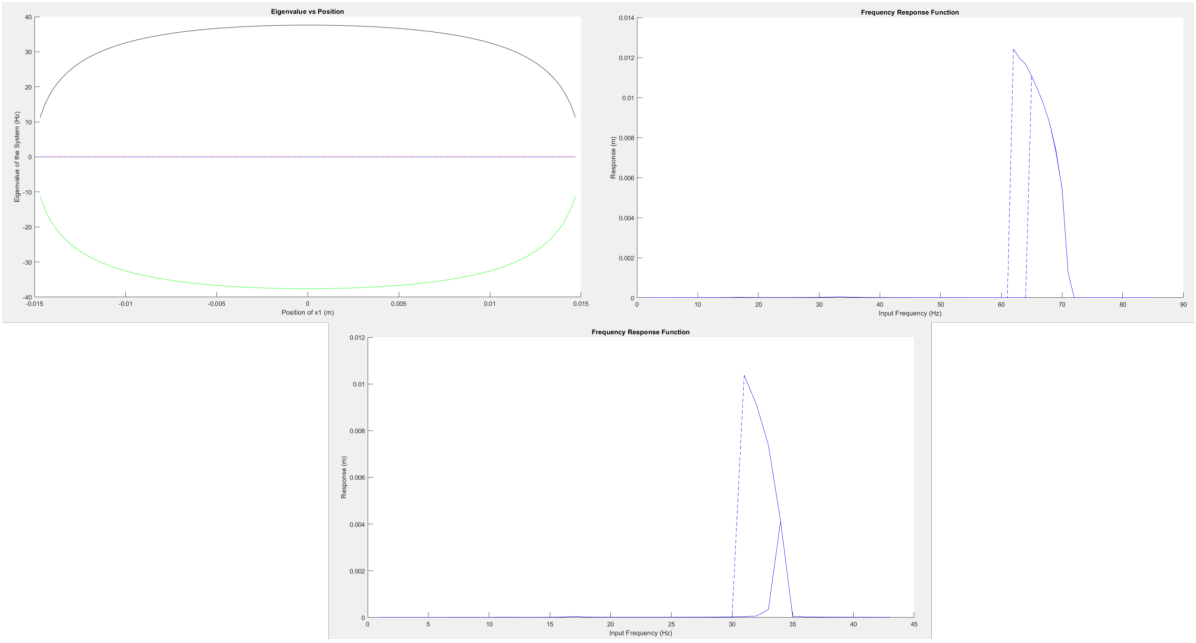


Figure 4.14: Frequency response function of prototype 2 with wing connection elements and wings.

## 4.2. Wings

As stated before, to produce the wings, it was chosen to use vacuum forming. For this a manual device was used, consisting of a base tray, a heating plate, a clamp and a vacuum pump. The film is clamped and suspended close to the heating plate. This heats the film and eventually makes it pliable. The clamp is then moved down and the vacuum pump activated. This forces the film into the tray, forming over any mold placed in it.

Thicker sheets of mylar sag slowly, being ready to form once the film would hit the mold in the tray when the clamp is moved down. Thinner sheets of mylar have a tendancy to shrink and shrivel when heated. This results in the material tearing if clamped in place. As such, for thinner films of mylar, it is adviced to only clamp the material once it is ready to be formed over the mold. Moreover, thinner films of mylar do not sag to indicate it is ready to be formed. Instead, thinner films discolour and become initially opaque, before returning to be clear. Once the material is clear, it is ready to be molded, but, if heated for too long, will quickly tear. As such, forming thinner films of mylar with this setup is challenging.

Depending on the quality of the edge, how well it conforms to the outer edge of the mold, it can be challenging to cut the wing free neatly. It is likely that at this stage, excess material is left on the wing, increasing its overall weight.

Wings of various thicknesses were produced for the project. To bring the wing mass under the initially desired 0.075 grams, a film of 50-75 micrometers is required. As, at these thickness, the manufacturing process is complicated, a set of wings with a thickness of 200 micrometers was also produced. A graph of the wing masses sorted by thickness can be found in Figure 4.15.

### 4.2.1. Wing Mold

For the mold, an iterative design was chosen as mentioned in the previous chapter, allowing for the evaluation of the limits of the process, as well as the resulting wing. This has an advantage over a theoretical approach, as it generates both expertise in the manufacturing method and gives tangible feedback on a design's weak points. The results of the iterative process can be found in Figure 4.16. The following subsections will elaborate, in short, what changed between the wing designs and why. The first four designs were intended to test the limits and capabilities of the molding process. The fifth design and later were resultant from that process. Each mold has holes in it to allow a vacuum to form on the inside of the mold after it has been sealed off by the plastic during the molding process. Marked in red are the identified folding lines. In Figure 4.17 some examples can be seen of finished wings of varying quality.

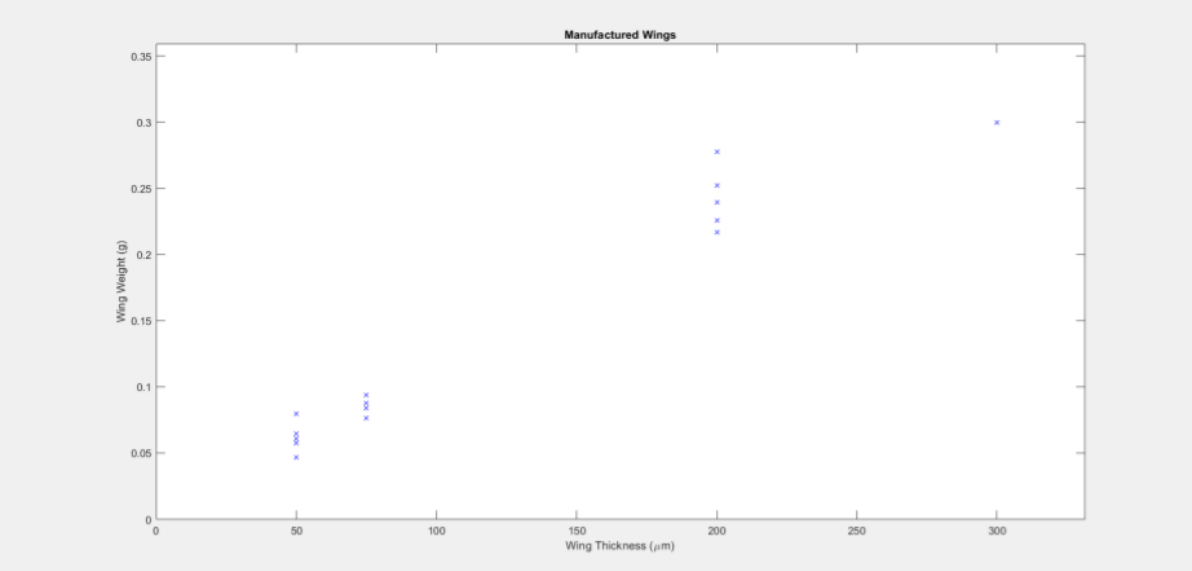


Figure 4.15: Measured weights of the manufactured wings.

Mark I
For the initial designs, it was decided to create clear weak points in the central folds. This would give an indication of the initial strength of the wing at a certain thicknesses as a result of the enclosing fold. This quickly proved insufficient for even the thicker films to be rigid under low stress.

Mark II
The second design attempted to reduce the folding weakness of the first design. Instead, this version proved suitably rigid under low stresses, but would buckle at the far ends of the vertical fold. This is as expected as the vertical fold represents a weak point in the rigidity. It was also found that any gap of one millimeter or smaller would be insufficiently large for the vacuum forming to be effective.

Mark III
The third design opted to explore curved folds instead. This version lacked reinforcement above the center-line and was improved to the fourth version without being produced. Additionally, the minimum size of a feature was identified to be at around 1 millimeter. As such, the holes were enlarged.

Mark IV
The fourth design had the same intend as the third, but, by adding an extra fold, was intending to increase rigidity along the vertical direction. This design proved weak to folding along the central horizontal axis, specifically above the lower fold and below the upper fold. The holes facilitating the vacuum within the mold were also up scaled to one millimeter, as it was found that details of that size were barely noticeable.

Mark V
Having explored the behaviour and limits of the production method, the fifth design improved on the curved design of the fourth by originating the second fold from the end of the first and extending it back past the root. This both reinforced the horizontal folding observed before and reinforced the area around the root of the wing. This design proved more rigid in all directions, but would still suffer buckling along the connection point.

Mark VI
The sixth design attempted to reinforced the weak point identified in the fifth design by adding an extra fold along the connection point. This proved to be the most rigid design yet, but, when reducing the thickness of the wing to 0.05 mm, would still fail to be rigid enough under high frequency load.

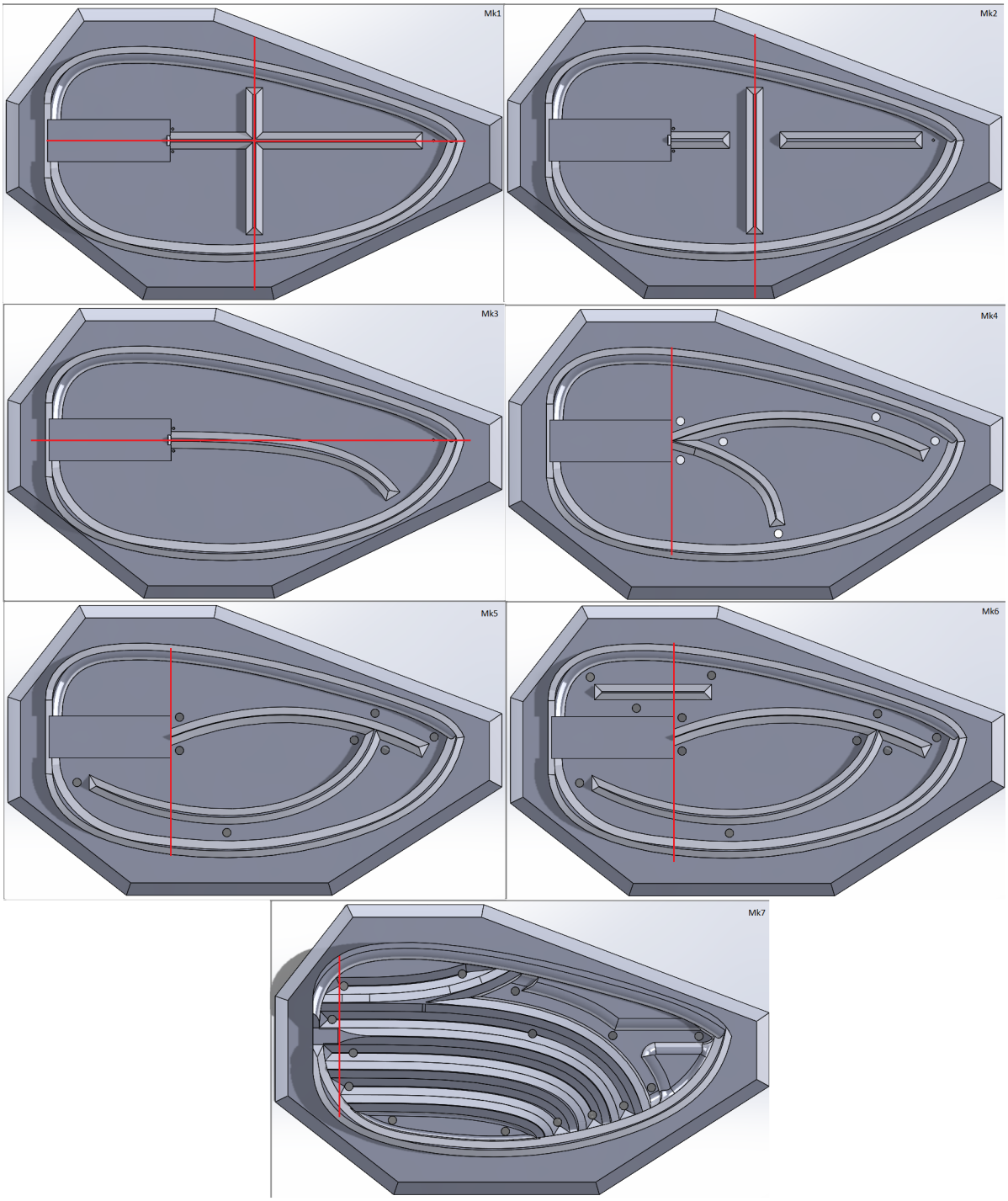


Figure 4.16: Various wing designs for vacuum forming with identified fold lines marked in red.

### Mark VII

The seventh design integrated the ideas from the previous versions and applied them along the entire plane and included the downward direction. This proved to be the most rigid version by far, but would still suffer failure at the connection point with the hinge at the root, despite the length of this being reduced. To overcome this, the hinge was changed to include a reinforcement as the base. This proved effective for the thicker films, but still ineffective for films under 100 $\mu$m.

Figure 4.17: Various produced mark IV wings of varying thicknesses and production qualities.

### 4.2.2. Wing Testing

The first wing that was properly tested was the mark IV wing. The following test setup was used; a dc-motor is attached to a wheel. This wheel is connected, via a crossbeam to another wheel, causing it to oscillate at certain amplitudes. A schematic of this setup can be found in Figure 4.18. By varying the input voltage of the dc-motor, a wide range of flapping frequencies can be reached. The frequency used for testing was around 30 Hz. A high speed camera was used to record the wings as they underwent the stresses of the motion.

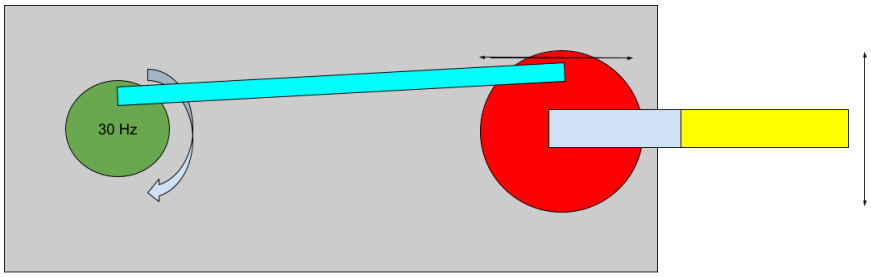


Figure 4.18: Test setup used to test the wing designs. Green: DC-motor driven wheel. Blue: Cross beam. Red: Wing mount. Light Blue: Wing connector. Yellow: Wing.

The mark IV wing, at a thickness of 50 and 75 $\mu$m, exhibits severe bending at the connection point of the wing, as the wing would bend a full 90 degrees. It was initially thought that by moving this point further from the pivot point would reduce this bending. This was done by locking the wing between two foam beams of 2 centimeters long. This solution did not solve the bending.

The mark V and VI attempted to address this by directly reinforcing this fold line. This helped at lower frequencies, but would still exhibit close to 90 degrees bending close to a 30 Hz stroke. As such, the mark VII was designed, using the entire surface for folds, rather than singular fold along the wing's spine. Additionally, valleys were introduced into the mold adding folds in the other direction as well. This again increased the frequency range before bending occurred, but would still fail when approaching 30 Hz. Finally, a test with

a hinge was added to the wing. It was hypothesised this would reduce the bending force along the plane of the wing by tilting it slightly. On top of this, a slight ridge was added to the hinge, reinforcing the connection point. The hinge seemed to have a positive effect, but would still experience bending when approaching 30 Hz. The ridge also had a positive effect, moving the bending point to the end of the ridge.

As the mark VII wings with a thickness of 200 $\mu$m did not bend this severely, not perceptibly bending, it was decided to make wings of this thickness instead. This is expected to reduce the efficiency of the design significantly, but not as significantly as the wings failing to remain rigid. The masses of these wings can be found in table 4.3

| Wing Nr | Mass (g) |
|---|---|
| 1 | 0.2778 |
| 2 | 0.2520 |
| 3 | 0.2260 |
| 4 | 0.2396 |

Table 4.3: Wing masses for the final design.

## 4.3. Hinges

As mentioned in chapter 3, for the hinge, a three piece cross axis pivot hinge is used. Using a sharp knife, three strips of 0.01 millimeters leafspring were cut. Two with a width of 3 millimeters and one with a width of 6 millimeters. For this, a small tray was printed with groves at the appropriate intervals. The length of these strips had to exceed 4 centimeters.

To create the hinge itself, two 3D prints were made. After the first layer of these prints was finished, the print would be paused and the strips would be placed over top, using two-sided tape. The print would then be resumed, fixing the strips at the appropriate length within the print. Once the print finished, the excess length of the springs was removed. Finally, the two prints were affixed to one another, using cyanoacrylate glue. A glass is placed on top, to ensure the pieces properly adhere. As part of the pieces, notches are included, allowing them to be aligned correctly. A schematic of this process can be found in Figure 4.19.

A triangular grove is printed at the ends of one of the pieces. This is meant to overlap with the wing, increasing the rigidity of the connection point.

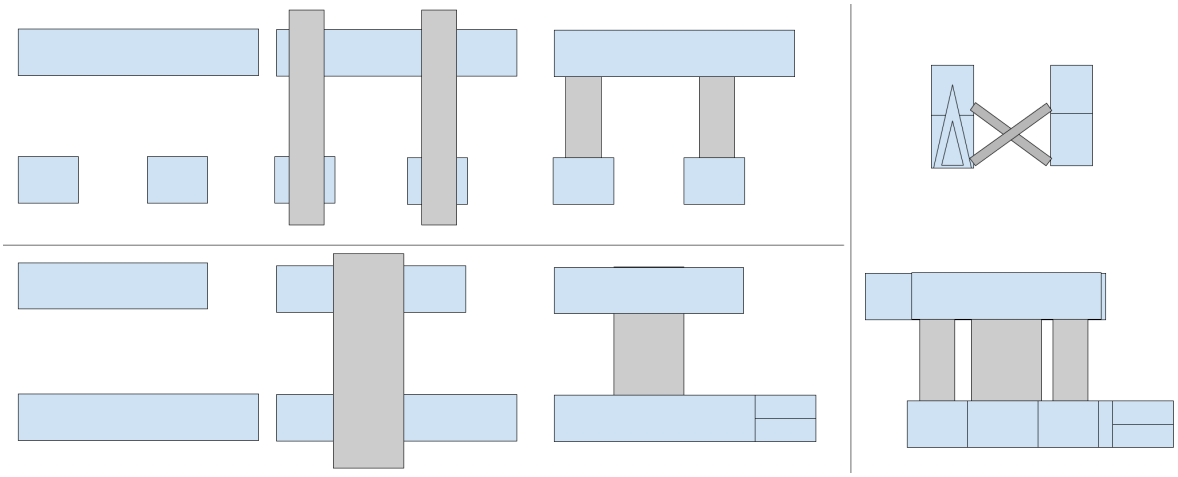

Figure 4.19: Manufacturing steps of the hinges.

Four hinges were designed in this way. The weight of this component is less critical than that of the wing, being placed far from the centre of mass of the wing and close to the pivot point of the system. As more weight reduces the efficiency of the design, however, it is still important that these parts are relatively low mass. The masses for the hinges used in the design can be found in Table 4.4. An image of the produced wings can be found in Figure 4.20

| Hinge Nr. | Mass (g) |
|---|---|
| 1 | 0.3051 |
| 2 | 0.3003 |
| 3 | 0.3132 |
| 4 | 0.3072 |

Table 4.4: Hinge mass values.

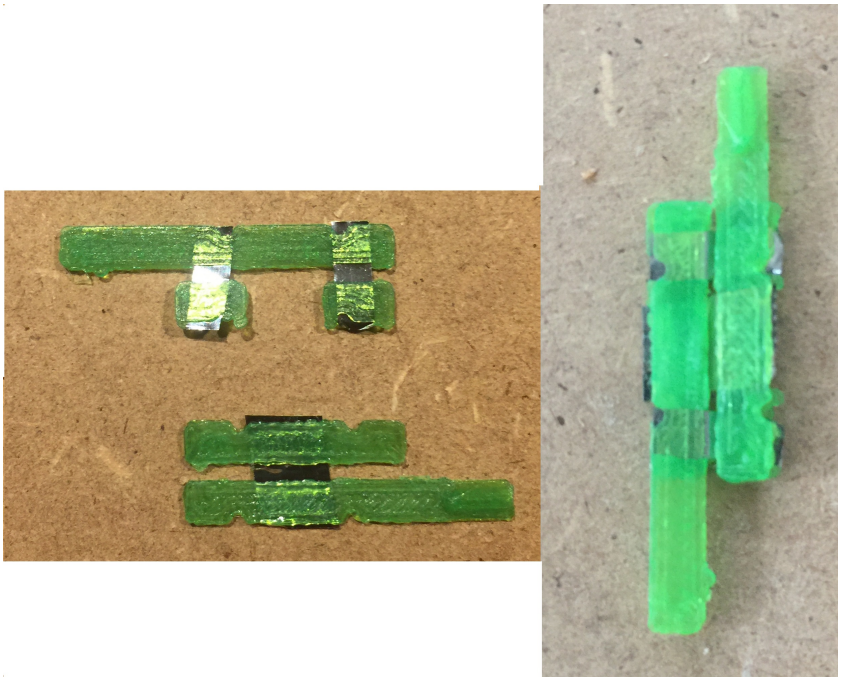

Figure 4.20: Fabricated prototype hinge.

## 4.4. Flying Prototype

The parameters of the theoretical prototype can now be assembled in Table 4.5.

It can now also be determined if the prototype could theoretically fly. The formula for the power generated by the actuator is

$$P = d * F * f. \tag{4.8}$$

Here d is the stroke length, F is the actuator force and f is the actuator frequency. Filled in, using ounches and inches, as provided by the datasheet and adjusting for the linear frequency divider gives the following result:

$$P = 0.0254 * 0.278 * 16 * 0.3/2 * 33.84 * 2 = 1.15W. \tag{4.9}$$

A duty cycle of 1/10 is used to obtain this estimated power, which means the actuator could only be used for about two seconds. This time is increased due to the effects of the actuator core passing through the actuator, but not by a reliable amount.

The found value can be compared to the expected losses found for the total weight.

$$L = 18.58/1000 * 38.4 = 0.713W. \tag{4.10}$$

As such, it can be concluded that, short of losses, the prototype could theoretically fly for short bursts. The final version of the flapping wing micro air vehicle can be found in Figure 4.21 and the built prototype in Figure 4.22.

| Parameter | Value |
|---|---|
| Vehicle Weight | 18.58 g |
| Optimal Frequency | 33.84 |
| Losses | 38.4 W/kg |
| $d_t$ | 0.499 |
| $d_r$ | 0.316 |
| Sweeping Amplitude | $1/3\pi$ |
| Wing Mass | 24e-5 kg |
| Number of Wings | 4 |
| Wing Span | 18.2 cm |

Table 4.5: Caption

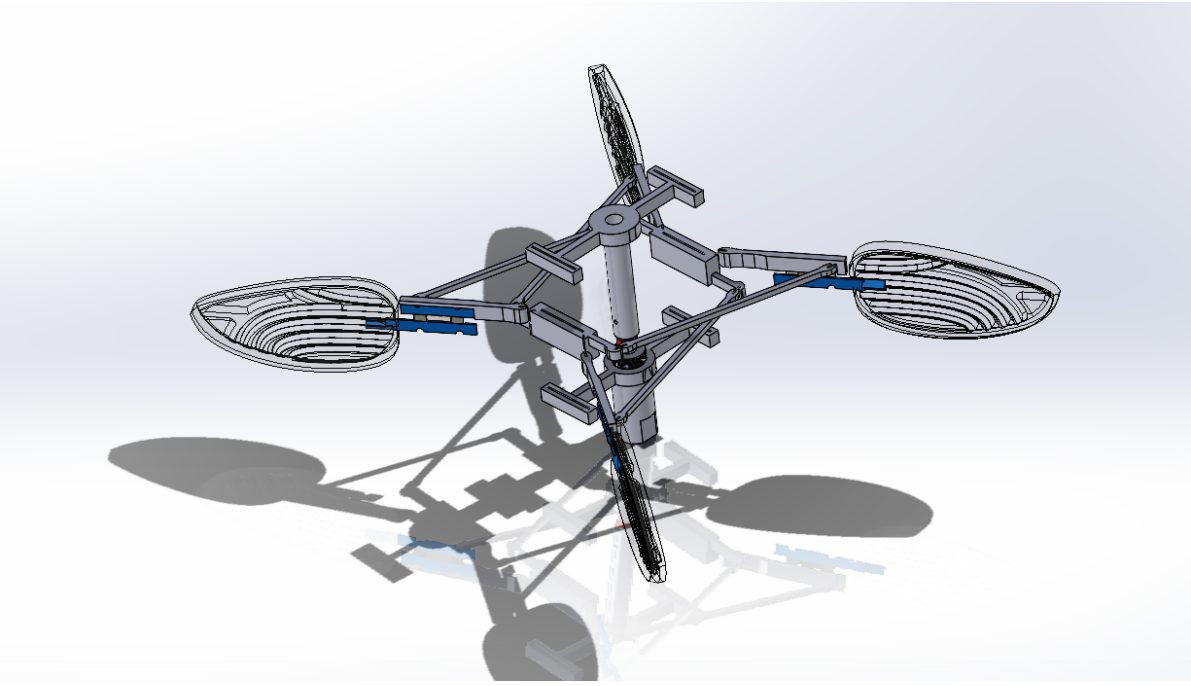

Figure 4.21: Final theoretical prototype of a flapping wing micro air vehicle using resonance and a linear frequency divider. The leaf springs are omitted.

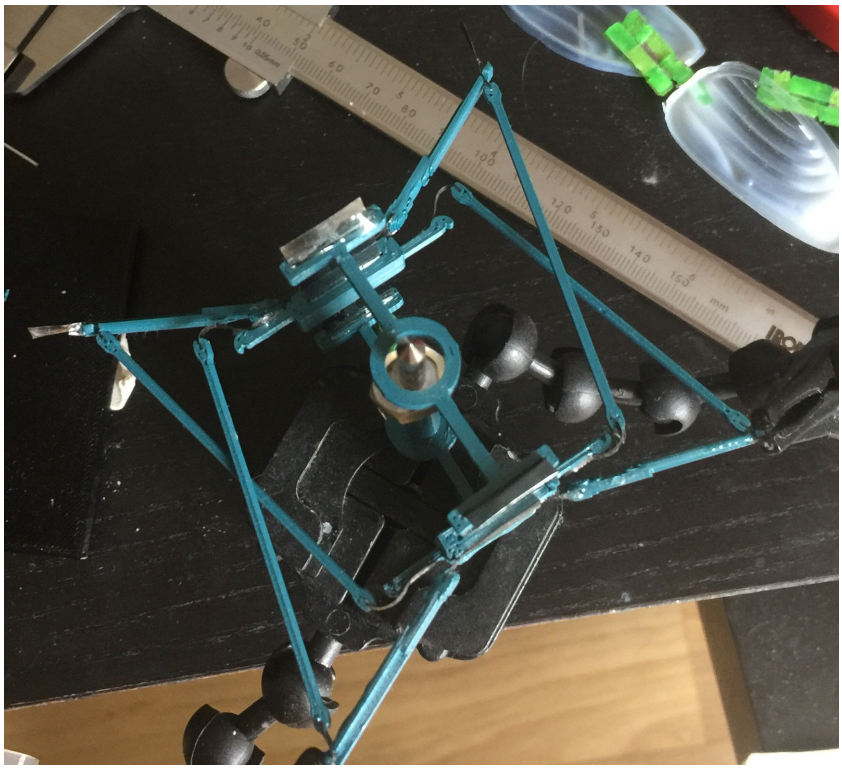

Figure 4.22: Last produced prototype. The mass meant to hold the actuator is facing the camera in this image.

# 5

# Conclusion and Recommendations

The following chapter discusses the results found in the previous chapter and lays out recommendations for any further studies conducted in this field. Particularly, the wings, linear frequency divider and flight capability will be discussed.

## 5.1. Wings

Vacuum forming can effectively be used to create a wing of a predetermined size and can even be used to reinforce a membrane through the introduction of folds. Reduction in thickness reduces the stiffness of such wings significantly, as expected. This project failed to create a wing of sufficient stiffness that was thinner than 200 $\mu$m using mylar. It was also observed that the wings varied in weight. It is believed that this variant is mainly the result of the quality of the edge formation. The better the outer edge of the wings forms, the less extra material is left at the edges, thus reducing the weight. A major shortcoming of the setup used for the vacuum forming was the lack of control, leaving room for large operator errors.

Future studies could investigate other materials than mylar, allowing for either more consistent manufacturing, less density in the material or better stiffness characteristics. Alternatively, a thin film of mylar could be vacuum formed and reinforced using plastics or metals, allowing the film to form the edge of the wing, but also reinforcing the weakest points. This would bring the wings closer to those found in insects. Also of benefit would be the improvement of the manufacturing setup. The current setup involves an operator either timing the heating of the material or monitoring it visually. Both of these methods lead to inconsistencies in the manufacturing, the first when the air humidity changes and when multiple wings are produced at once, the second as it relies on the operator's skill with the setup. These errors become more pronounced with thinner films of material.

Another thing to consider is that the design presented in this paper is by no means an optimal wing, merely a design that proved most rigid from the ones tested. As such, it could well be worth exploring an improvement to the mold as well. As the material becomes thinner, however, the effects of fold decreases. As such, one of the previous suggestions might prove more effective.

## 5.2. Linear Frequency Divider

For increasing the output of a linear solenoid, without affecting the output frequency, a linear frequency divider looks promising. The system responds uniformly across the operating area and can be tuned with some accuracy. Two working prototypes have been constructed using error sensitive construction methods. This shows that, despite having some sensitivities to manufacturing errors, the divider can be constructed without the need for expensive machinery. Most asymmetries are lost when the divider is operated at the appropriate frequencies.

Further studies could focus on the manufacturing methods of the linear frequency divider itself, as well as improving the methods by which elements can be connected to it. Furthermore, the power loss of this system has only been briefly evaluated using a Q-factor analysis, but further testing in regards to the system's reactions to greater damping effects should prove meaningful. A version could even be constructed with an adjustable design, allowing the output frequency to be adjusted by increasing or decreasing the stiffness of

the springs. Finally, work could be done to reduce the size of the divider, as it currently causes the wingspan of the prototype to exceed the desired maximum wingspan.

## 5.3. Flight Capability

Theoretically, the prototype seems to be able to fly as a result of the linear frequency divider. Of course, this does require a version to be built that is sufficiently power efficient. Due to the capabilities of the used actuator, this theoretical flight also requires the actuator to be run on a low duty cycle, limiting the duration of any flight.

Further studies could focus on the improvement of the used actuator, the development of a two stage linear frequency divider, the reduction of the weight of the components, or the optimisation of the used space of the linear frequency divider. The effectiveness of each of these directions varies, with the greatest efficiency gains being in the actuator and the second stage linear frequency divider. Both could increase the loss to weight ratio by around 25%.

# Bibliography


[1] D. Floreano R. J. Wood. Science, technology and the future of small autonomous drones . (English). Nature, 521(7553):60–466, 2015.

[2] T. A. Ward C. J. Fearday E. Salami N. B. Soin. A bibliometric review of progress in micro air vehicle research . (English). International Journal of Micro Air Vehicles, 9(2):146–165, 2017.

[3] H. Liu S. Ravi D. Kolomenskiy H. Tanaka. Biomechanics and biomimetics in insect-inspired flight systems. (English). Philosophical Transactions of the Royal Society B: Bio-logical Sciences, 371(1704), 2016.

[4] M. Karasek F. T. Muijres C. de Wagter B.D.W. Remes G.C.H.E. de Croon. A tailless aerial robotic flapper reveals that flies use torque coupling in rapid banked turns. (English). Science, 361(6407):1089–1094, 2018.

[5] N. T. Jafferis E. F. Helbling M. Karpelson R. J. Wood. Untethered flight of an insect-sized flapping-wing microscale aerial vehicle. (English). Nature, 570:491–495, 2019.

[6] S. Deng M. Percin B. Van Oudheusden B. Remes H. Bijl. Experimental Investigation on the Aerodynamics of a Bio-Inspired Flexible Flapping Wing Micro Air Vehicle . (English). International Journal of Micro Air Vehicles, 6(2):105–115, 2014.

[7] C. T. Bolsman. Flapping wing actuationusing resonant compliant mechanisms: An insect-inspired design. (English). 2010.

[8] D. Coleman M. Benedict V. Hrishikeshavan I. Chopra. Design , Development and Flight-Testing of a Robotic Hummingbird . (English). American Helicopter Society 71st Annual Forum, 2015.

[9] M. Ras. Design, Fabrication and Assembly of a Flapping-Wing with Integrated Compliant Hinge: Application in a Bio-Inspired, Resonant Micro Air Vehicle . (English). 2020.

[10] J. M. Grasmeyer M. T. Keennon. Development of two mavs and vision of the future of mav design . (English). AIAA International Air and Space Symposium and Exposition: The Next 100 Years, page 2901, 2003.

[11] E. Steltz S. Avadhanula R.S. Fearing. High Lift Force with 275 Hz Wing Beat in MFI . (English). IEEE International Conference on Intelligent Robots and Systems, page 3987–3992, 2007.

[12] Q. V. Nguyen H. C. Park N. S. Goo D. Byun. A flying insect-like flapper actuated by a compressed LIPCA . (English). IEEE International Conference on Robotics and Automation, 15(18):19–24, 2007.

[13] V. Q. Nguyen M. Syaifuddin H. C. Park D. Y. Byun N. S. Goo K. J. Yoon. Characteristics of an insect-mimicking flapping system actuated by a unimorph piezoceramic actuator . (English). Journal of Intelligent Material Systems and Structures, 19(10):1185–1193, 2008.

[14] R. J. Wood. The first takeoff of a biologically inspired at-scale robotic insect . (English). IEEE Transactions on Robotics, 24(2):341–347, 2008.

[15] S. S. Baek K. Y. Ma R. S. Fearing. Efficient Resonant Drive of Flapping-Wing Robots . (English). 2009 IEEE/RSJ International Conference on Intelligent Robots and Systems, page 2854–2860, 2009.

[16] G. C. De Croon M. A. Groen C. De Wagter B. Remes R. Ruijsink and B. W. Van Oudheusden. Design, aerodynamics and autonomy of the DelFly . (English). Bioinspiration and Biomimetics, 7(2), 2012.

[17] M. Keennon K. Klingebiel H. Won. Development of the Nano Hummingbird: A Tailless Flapping Wing Micro Air Vehicle . (English). 50th AIAA Aerospace Sciences Meeting including the New Horizons Forum and Aerospace Exposition, 2012.

[18] K. Y. Ma P. Chirarattananon S. B. Fuller R. J. Wood. Controlled Flight of a Biologically Inspired, Insect-Scale Robot . (English). Science, page 603–607, 2013.

[19] M. Azhar D. Campolo G. K. Lau L. Hines M. Sitti. Flapping wings via direct-driving by DC motors . (English). IEEE International Conference on Robotics and Automation, 6(10):1397–1402, 2013.

[20] L. Hines D. Campolo M. Sitti. Liftoff of a motor-driven, flapping-wing microaerial vehicle capable of resonance . (English). IEEE Transactions on Robotics, 30(1):220–232, 2014.

[21] L. Ristroph S. Childress. Stable hovering of a jellyfish-like flying machine . (English). Journal of The Royal Society Interface, 11(92), 2014.

[22] L. Hines. Design and Control of a Flapping Flight Micro Aerial Vehicle . (English). 2014.

[23] L. Hines D. Colmenares M. Sitti. Platform design and tethered flight of a motor-driven flapping-wing system . (English). Proceedings - IEEE International Conference on Robotics and Automation, 26(30):5838–5845, 2015.

[24] M. H. Rosen G. le Pivain R. Sahai N. T. Jafferis R. J. Wood. Development of a 3.2g Untethered Flapping-Wing Platform for Flight Energetics and Control Experiments . (English). IEEE International Conference on Robotics and Automation, page 3227–3233, 2016.

[25] H. V. Phan S. Aurecianus T. Kang H. C. Park. Design, aerodynamics and autonomy of the DelFly . (English). Bioinspiration and Biomimetics, 12(3), 2017.

[26] A. Roshanbin H. Altartouri M. Karásek A. Preumont. COLIBRI: A hovering flapping twin-wing robot . (English). International Journal of Micro Air Vehicles, 9(4):270–282, 2017.

[27] C. Cao S. Burgess A. T. Conn. Toward a Dielectric Elastomer Resonator Driven Flapping Wing Micro Air Vehicle . (English). Frontiers in Robotics and AI, 5, 2019.

[28] H. Deng S. Xiao B. Huang L. Yang X. Xiang X. Ding. Design optimization and experimental study of a novel mechanism for a hover-able bionic flapping-wing micro air vehicle . (English). Bioinspiration Biomimetics, 16(2), 2020.

[29] T. Ozaki K. Hamaguchi. Improved lift force of a resonant-driven flapping-wing micro aerial vehicle by suppressing wing–body and wing–wing vibration coupling . (English). Extreme Mechanics Letters, 40:100867, 2020.

[30] T. Jimbo T. Ozaki Y. Amano K. Fujimoto. Flight control of flapping-wing robot with three paired direct-driven piezoelectric actuators . (English). Elsevier, 53(3):9391–9398, 2020.

[31] M. Ras. Design, Fabrication and Testing of a Resonant Flapping-Wing Micro Air Vehicle . (English). 2019.

[32] Q. Wang. Modeling, Design and Optimization of Flapping Wings for Efficient Hovering Flight. (English). 2017.

[33] H. J. Peters. A CONTROLLABILITY APPROACH FOR RESONANT COMPLIANT SYSTEMS: APPLIED TO A FLAPPING WING MICRO AIR VEHICLE DESIGN. (English). 2016.

[34] A. Amer. Shape Optimization of a Flapping Wing for the Atalanta Project FWMAV. (English). 2021.

[35] I.Sher D.Levinzon-Sher E.Sher. Miniaturization limitations of HCCI internal combustion engines . (English). Applied Thermal Engineering, 29(2-3):400–411, 2009.

[36] S. P. Burugupally L. Weiss. Design and performance of a miniature free piston expander . (English). Energy, 170:611–618, 2018.

[37] G. Mous. A miniature chemical actuator with a compliant expansion chamber, passive exhaust valve and electrowetting-based fuel injection . (English). 2020.

[38] S. Roundy E. S. Leland J. Baker E. Carleton E. Reilly E. Lai B. Otis J. M. Rabaey P. K. Wright V. Sundararajan. Improving power output for vibration-based energy scavengers . (English). IEEE Pervasive Computing, 4(1):28 – 36, 2005.

[39] Y. Bar-Cohen. Electroactive Polymer (EAP) Actuators as Artificial Muscles: Reality, Potential, and Challenges, 2nd edition . (English). SPIE–The International Society for Optical Engineering, 2004.

[40] S. Büttgenbach S. Bütefisch M. Leester-Schädel A. Wogersien. Shape memory microactuators . (English). Microsystem Technologies, 7(4):165–170, 2001.

[41] P. van Esch S. Nieuwenhuis L. N. van Driessen E. Le Blansch. A Compliant Mechanical Frequency Dividing Transmission Using Parametric Oscillation . (English). 2019.

[42] N.K. Teunisse. Maximization of the geometric non-linearities of a thin-walled structure in resonance . (English). 2015.

[43] G. Mous. The challenges of using actuators in FMWAV: a review and technical analysis . (English). 2020.

# A

# Atalanta Overview Table

| Title | Type | Year | Subject | Reference |
|---|---|---|---|---|
| Design, Fabrication and Testing of a Resonant Flapping-Wing Micro Air Vehicle | Literature Study | 2019 | Assembly | [31] |
| FWMAV TEST SIMULATOR | BEP | 2013 | Assembly, Simulation | |
| Flapping wing actuation using resonant compliant mechanisms: An insect-inspired design | PhD Thesis | 2010 | Assembly | [7] |
| A miniature chemical actuator with a compliant expansion chamber, passive exhaust valve and electrowetting-based fuel injection | Master Thesis | 2020 | Actuator, Chemical | [37] |
| The challenges of using actuators in FMWAV: a review and technical analysis | Literature Study | 2020 | Actuator | [43] |
| A Compliant Mechanical Frequency Dividing Transmission Using Parametric Oscillation | BEP | 2019 | Actuator, Transmission | |
| Conceptual development of a catalytic expansion actuator for a resonating-body flapping-wing micro air vehicle | Master Thesis | 2015 | Actuator, Chemical | |
| Ontwerp van een FWMAV actuator | BEP | 2013 | Actuator, Electric | |
| Design analysis for a small scale hydrogenperoxide powered engine for a Flapping Wing Mechanism Micro Air Vehicle | Master Thesis | 2012 | Actuator, Chemical | |
| High energy density micro-actuation based on gasgeneration by means of catalysis of liquid chemicalenergy | Master Thesis | 2010 | Actuator, Chemical | |
| Resonating structures with flapping wings: Numerical modelling and validation | Master Thesis | 2016 | Controllability, Steering | |
| A Controllability Approach for Resonant Compliant Systems Applied to a Flapping Wing Micro Air Vehicle Design | PhD Thesis | 2015 | Controllability, Steering | |
| Maximization of the geometric non-linearitiesof a thin-walled structure in resonance | Master Thesis | 2015 | Controllability, Flap-Motion | [42] |
| Dynamic Analysis of a Resonance Based Micro Air Vehicle Structure | Master Thesis | 2014 | Controllability, Flap-Motion | |
| Resonating Response Modifications of Compliant Structures Induced by Structural Changes | Master Thesis | 2013 | Controllability, Steering | |
| Shape Optimization of a Flapping Wing for the Atalanta Project FWMAV | Master Thesis | 2021 | Wing, Design/Production | [34] |
| Design, Fabrication and Assembly of a Flapping-Wing with Integrated Compliant Hinge: Application in a Bio-Inspired, Resonant Micro Air Vehicle | Master Thesis | 2020 | Wing, Design/Production | [9] |
| Design of a Flapping Wing for Application in a MAV | Master Thesis | 2019 | Wing, Design | |
| Modeling, Design and Optimization of Flapping Wings for Efficient Hovering Flight | PhD Thesis | 2017 | Wing, Hinge | [32] |
| Out-of-plane motions of insects for flapping wing micro air vehicles | BEP | 2014 | Wing, Hinge | |
| WING MANUFACTURE FOR MICRO AERIAL VEHICLES USING ADDITIVE MANUFACTURING TECHNIQUES | BEP | 2013 | Wing, Production | |
| The Optimization of the Flapping Wings for a Micro Air Vehicle | Master Thesis | 2011 | Wing, Design | |
| ATALANTA VLEUGEL 2 | Literature Study | 2007 | Wing, Design/Testing | |
| Atalanta Vleugel: Een onderzoek in het kader van het Devlab –Atalanta project | Master Thesis | 2006 | Wing | |
| Development of Optical System for Autonomous flight of Atalanta Micro Aerial Vehicle: Vision intelligence using Optical-Flow based Control Strategies | Literature Study | 2020 | Control, Optics | |
| Flight control Simulator using Optic-flow Hardware-in-the-loop (HITL) | Master Thesis | 2020 | Control, Optics | |
| Flight Control and Collision Avoidance for Quadcopter and Flapping-Wing MAVs using only Optical Flow: Theory, Simulation and Experiment | Master Thesis | 2018 | Control, Optics | |
| CONTROLLING THE BENDING STIFFNESS OF A CANTILEVER HINGE | BEP | 2015 | Control, Steering | |
| Optic flow karakteristiek van eenoptische muis sensor | BEP | 2014 | Control, Optics | |
| Simulation of optic flow basedflight control for a flapping wingmicro aerial vehicle | Master Thesis | 2014 | Control, Simulation | |
| Structural control method research motivated for MAV lift force modification | Master Thesis | 2013 | Control, Steering | |
| Wing control of a Flapping Wing Micro AirVehicle (FWMAV) using piezoelectrics | BEP | 2013 | Control, Steering | |

# B

# Equations of Motion

For the formulation of the equations of motion, the following assumptions are mode: $m_1$ and $m_2$ have opposing positions and are always at the same height. The angle of the leaf springs relative to the masses will be equal. $m_b$ and $m_t$ do not move in the x-direction.

$$x_1 = -x_2 \tag{B.1}$$
$$y_1 = y_2 \tag{B.2}$$
$$\alpha = \beta \tag{B.3}$$
$$x_b = x_t = 0 \tag{B.4}$$

These assumptions leave the following position elements as the second mass can effectively be ignored:

$$x = \begin{bmatrix} x_1 \\ y_1 \\ y_t \\ y_b \end{bmatrix} \tag{B.5}$$

Now the total forces on each remaining mass can be evaluated. Here $k_l$ affects $x_1$ twice, as there are two leaf springs affecting $m_1$. Additionally, a reactant force is present along each of the leaf springs.

$$F_{x1} = -2 * (x_1 + c)k_l + F_{r_{x1}} \tag{B.6}$$
$$F_{y1} = F_{r_{y1}} \tag{B.7}$$
$$F_{yb} = F_{r_{yb}} \tag{B.8}$$
$$F_{yt} = F_{r_{yt}} \tag{B.9}$$

This results in the following equations of motion:

$$m_1 * \ddot{x_1} + 2 * (x_1 + c) * k_l - F_{r_{x1}} = 0 \tag{B.10}$$
$$m_1 * \ddot{y_1} - F_{r_{y1}} = 0 \tag{B.11}$$
$$m_b * \ddot{y_b} - F_{r_{yb}} = 0 \tag{B.12}$$
$$m_t * \ddot{y_t} - F_{r_{yt}} = 0 \tag{B.13}$$

Now the reactant forces can be rewritten as to eliminate two variables.

$$F_{r_{x1}} = sin(\alpha) * F_{r_b} + sin(\beta) * F_{r_t} \tag{B.14}$$
$$F_{r_{y1}} = -cos(\alpha) * F_{r_b} + cos(\beta) * F_{r_t} \tag{B.15}$$
$$F_{r_{yb}} = 2cos(\alpha) * F_{r_b} \tag{B.16}$$
$$F_{r_{yt}} = -2cos(\beta) * F_{r_t} \tag{B.17}$$

The angles can be expressed as dependant on $x_1$ and $y_1$:

$$\alpha = sin^{-1}(\frac{-x_1 - c}{L}) \tag{B.18}$$
$$\alpha = cos^{-1}(\frac{y_1 - y_b}{L}) \tag{B.19}$$
$$\beta = sin^{-1}(\frac{-x_1 - c}{L}) \tag{B.20}$$
$$\beta = cos^{-1}(\frac{y_t - y_1}{L}) \tag{B.21}$$

The equations of motions currently lack a connection between $m_b$, $m_t$ and $m_1$. As such, we need two additional constraint equations:

$$y_b = y_1 - L * cos(\alpha) \tag{B.22}$$
$$y_t = y_1 + L * cos(\beta) \tag{B.23}$$

In order to substitute the constraint equations in the equations of motion, the second time derivative needs to be taken:

$$\dot{y_b} = \dot{y_1} + \dot{\alpha} * sin(\alpha) * L \tag{B.24}$$
$$\ddot{y_b} = \ddot{y_1} + \ddot{\alpha} * sin(\alpha) * L + \dot{\alpha}^2 * cos(\alpha) * L \tag{B.25}$$
$$\dot{y_t} = \dot{y_1} - \dot{\alpha} * sin(\alpha) * L \tag{B.26}$$
$$\ddot{y_t} = \ddot{y_1} - \ddot{\alpha} * sin(\alpha) * L - \dot{\alpha}^2 * cos(\alpha) * L \tag{B.27}$$

As the intent is to express the final equations of motion in terms of $x_1$ and $y_1$, $\ddot{\alpha}$ needs to also be determined:

$$\dot{\alpha} = -\frac{\dot{x_1}}{L * \sqrt{1 - (\frac{-x_1 - c}{L})^2}} \tag{B.28}$$
$$\ddot{\alpha} = -\frac{\ddot{x_1}}{L * \sqrt{1 - (\frac{-x_1 - c}{L})^2}} + \frac{-(x_1 + c) * \dot{x_1}^2}{L^3 * (1 - (\frac{-x_1 - c}{L})^2)^{1.5}} \tag{B.29}$$

By substituting $\ddot{\alpha}$, the following formulas are obtained:

$$\ddot{y_b} = \ddot{y_1} - (x_1 + c) * (-\frac{\ddot{x_1}}{L * \sqrt{1 - (\frac{-x_1 - c}{L})^2}}) + \frac{-(x_1 + c) * \dot{x_1}^2}{L^3 * (1 - (\frac{-x_1 - c}{L})^2)^{1.5}} + (y_1 - y_b) * (\frac{\dot{x_1}}{L * \sqrt{1 - (\frac{-x_1 - c}{L})^2}})^2 \tag{B.30}$$
$$\ddot{y_t} = \ddot{y_1} + (x_1 + c) * (-\frac{\ddot{x_1}}{L * \sqrt{1 - (\frac{-x_1 - c}{L})^2}} + \frac{-(x_1 + c) * \dot{x_1}^2}{L^3 * (1 - (\frac{-x_1 - c}{L})^2)^{1.5}}) - (y_1 - y_b) * (\frac{\dot{x_1}}{L * \sqrt{1 - (\frac{-x_1 - c}{L})^2}})^2 \tag{B.31}$$

For the purpose the eigenvalue, the viscous elements are unnecessary. Setting $\dot{x_1}$ to zero gives:

$$\ddot{y_b} = \ddot{y_1} + (x_1 + c) * \frac{\ddot{x_1}}{L * \sqrt{1 - (\frac{-x_1 - c}{L})^2}} \tag{B.32}$$
$$\ddot{y_t} = \ddot{y_1} - (x_1 + c) * \frac{\ddot{x_1}}{L * \sqrt{1 - (\frac{-x_1 - c}{L})^2}} \tag{B.33}$$
$$\sqrt{L^2 - (x_1 + c)^2} = (y_1 - y_b) = (y_t - y_1) \tag{B.34}$$

Substituting B.32 and in and leaves the following equations:

$$m_1 * \ddot{x_1} + 2 * (x_1 + c) * k_l - \frac{(-x_1 - c)}{L} * (F_{r_b} + F_{r_t}) = 0 \tag{B.35}$$

$$m_1 * \ddot{y_1} + \frac{(y_1 - y_b)}{L} * (F_{r_b} - F_{r_t}) = 0 \tag{B.36}$$

$$m_b * (\ddot{y_1} + (x_1 + c) * \frac{\ddot{x_1}}{(y_1 - y_b)}) - 2 * \frac{F_{r_b} * (y_1 - y_b)}{L} = 0 \tag{B.37}$$

$$m_t * (\ddot{y_1} - (x_1 + c) * \frac{\ddot{x_1}}{(y_1 - y_b)}) + 2 * \frac{F_{r_t} * (y_1 - y_b)}{L} = 0 \tag{B.38}$$

$F_{r_b}$ and $F_{r_t}$ can be expressed using the following formulas derived from and

$$F_{r_b} = m_b * (\frac{\ddot{y_1} * L}{2 * (y_1 - y_b)} + \frac{\ddot{x_1} * (x_1 + c) * L}{2 * (y_1 - y_b)^2}) \tag{B.39}$$

$$F_{r_t} = m_t * (-\frac{\ddot{y_1} * L}{2 * (y_1 - y_b)} + \frac{\ddot{x_1} * (x_1 + c) * L}{2 * (y_1 - y_b)^2}) \tag{B.40}$$

Substituting $F_{r_b}$ and $F_{r_t}$ in and gives:

$$m_b - m_t = m_a \tag{B.41}$$

$$2 * m_1 * \ddot{x_1} + 4 * (x_1 + c) * k_l - m_a \frac{\ddot{y_1}(-x_1 - c)}{(y_1 - y_b)} - (m_b + m_t) \frac{\ddot{x_1} * (x_1 + c)^2}{(y_1 - y_b)^2} = 0 \tag{B.42}$$

$$(2 * m_1 + m_b + m_t) * \ddot{y_1} + m_a \frac{\ddot{x_1} * (x_1 + c)}{(y_1 - y_b)} = 0 \tag{B.43}$$

Using the above equations, the mass matrix and stiffness matrix can finally be found.

$$M = \begin{bmatrix} 2 * m_1 - (m_b + m_t) \frac{(x_1+c)^2}{(y_1-y_b)^2} & m_a \frac{(x_1+c)}{(y_1-y_b)} \\ m_a \frac{(x_1+c)}{(y_1-y_b)} & (2 * m_1 + m_b + m_t) \end{bmatrix} \tag{B.44}$$

$$K = \begin{bmatrix} 4 * k_l & 0 \\ 0 & 0 \end{bmatrix} \tag{B.45}$$